THE OCCURRENCE OF MAGNETIC PARTICULATE RESIDUES IN VEHICLE PROPANE TANKS

BY

EDWARD G. HOHENBERG

A Thesis
Submitted to the Faculty of Graduate
Studies in Partial Fullfillment of the
Requirements for the Degree of

MASTER OF SCIENCE

Department of Mechanical Engineering
University of Manitoba
Winnipeg, Manitoba

ISBN 0-315-77920-9

THE OCCURENCE OF MAGNETIC PARTICULATE RESIDUES IN VEHICLE PROPANE TANKS

BY

EDWARD G. HOHENBERG

A thesis submitted to the Faculty of Graduate Studies of the University of Manitoba in partial fulfillment of the requirements of the degree of

MASTER OF SCIENCE

ABSTRACT

An investigation was undertaken to study the occurrence of black magnetic particulate residues in motor vehicle propane storage tanks.

Residue samples were acquired from vehicle filters in a vehicle fleet test. All test vehicles had been fueled with propane under controlled conditions. Residues were examined with a Scanning Electron Microscope (SEM), and chemically analyzed using Energy Dispersive Spectroscopy (EDS) and X-Ray Diffraction (XRD). A decommissioned vehicle propane tank was also obtained, sectioned, studied with optical microscopy and a SEM, and sections analyzed using EDS and XRD.

SEM, EDS and XRD analysis showed the particulate residues to be predominantly magnetite (iron oxide) flakes. Examination and analysis of the inside of the decommissioned vehicle tank showed an iron oxide layer composed primarily of magnetite, and evidence of oxide layer spallation. The tank oxide layer was found to originate with the manufacture of the steel.

It was concluded that the particulate residues were due to spallation of the resident oxide layer within the

tank, and that residue generation could be prevented by elimination of the tank oxide.

ACKNOWLEDGEMENTS

The author would like to express his sincere appreciation to all those individuals and groups who helped make this thesis possible. Thanks firstly to Dr. J. R. Cahoon, the thesis advisor, for his assistance. Thanks to The Propane Gas Association of Canada for the financial assistance provided during this research project. Thanks to Tim Eaton who provided needed samples, and answered endless questions graciously. Lastly, the author wishes to acknowledge Sandra Smith, who provided significant motivation for the completion of this thesis. Thanks to all.

TABLE OF CONTENTS

List of Figures

List of Tables

CHAPTER 1 INTRODUCTION

1.1 Propane as a Vehicle Fuel

Recently, propane has become increasingly popular as a motor vehicle fuel. Higher octane, cleaner burning and lower cost are some of the major advantages over gasoline.

The basic vehicle propane fuel system consists of a storage tank, transfer and conversion system with filtration, and propane carburetor(s), as shown in Figure 1. Since propane for vehicle fuel applications is stored as liquefied propane under pressure, the storage vessel must adhere to Pressure Vessel Manufacturing Codes. The vehicle tanks are typically designed for specific vehicle applications, and built according to the ASME Pressure Vessel Code.

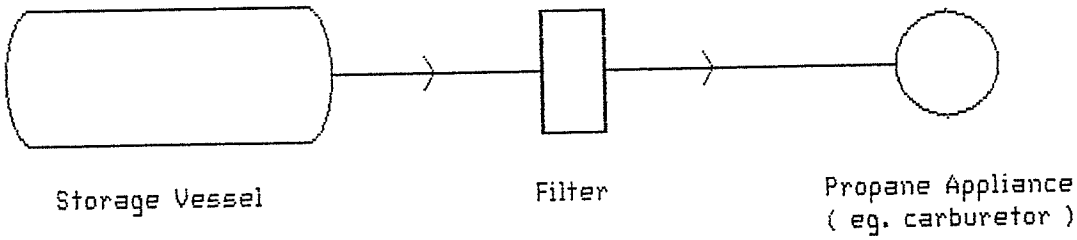

FIGURE 1 Propane Fuel System

1.2 The Particulate Residue Problem

In propane powered vehicles, the propane is drawn out of the storage vessel in a liquid state. Consequently, any particulate residues, which may have been stirred into suspension in the liquid propane, are also drawn out. In-line filters will stop particles 12-20μm in size, but finer particles will be passed on to the propane liquid vapor converter, and to the appliance (carburetor).

In the early 1980's, large amounts of black magnetic residues were discovered in the in-line filters of some propane powered vehicles. In severe cases, the filters became clogged with residue. In any case, the presence of the black residues could lead to operational problems of propane vaporizers, regulators and carburetors.[1] Also, the presence of hard magnetic particulate residues could cause inadequate sealing of solenoid operated closure valves.

1.3 Objectives

In 1986 the Propane Gas Association of Canada (PGAC) formed a Propane Magnetic Residue and Odourant Committee to investigate the residue problem, as well as an

odourant fade problem. In 1987 a fleet test of Department of National Defence (DND) propane powered vehicles was undertaken to collect, under controlled conditions, analysis samples of the magnetic residues, as well as gather statistical data on the vehicles (mileage, etc.).

The research objectives of this thesis were to use the DND fleet test data and residue samples, as well as a decommissioned vehicle propane tank, to investigate the occurrence of the black magnetic residues, to draw conclusions as to the cause of the residues, and to propose a solution to the problem.

CHAPTER 2 EXPERIMENTATION

2.1 Overview

In order to investigate the occurrence of the propane residues, the following experimentation was performed:

1. Chemical analysis of the DND fleet test residue samples.

2. Chemical analysis of selected miscellaneous residue samples.

3. Sectioning of a decommissioned propane vehicle tank, for analysis of the tank walls, and inner structures.

2.2 Residue Analysis

2.2.1 The DND Fleet Test Samples

In 1988, 13 DND propane powered vehicles were selected to be part of a fleet test initiated by the PGAC odourant and residue committee to collect residue samples under controlled conditions. All the selected vehicles were in

continuous service on a variety of duty cycles in the Winnipeg area.

All vehicles in the test group were filled with propane from the same source, and all propane was filtered to at least 10 μm on introduction into the test vehicle tanks. Test vehicle propane storage tanks were also fitted with a redundant fuel lockoff to prevent the introduction of any contaminants into the empty storage tanks.

In-line filters were changed regularly, with service mileage and dates recorded for each used filter. Upon removal from the vehicles, all used filters were immediately placed in sealed zip-lock bags to prevent contamination of the collected residues from environmental sources.

The DND vehicle fleet test produced 63 used in-line propane filters, of which 13 filters had sufficient residue deposits for analysis.

Table 1 lists the vehicle data for the fleet test. All storage tanks were constructed of steel except for the Worthington manufactured tank, which was constructed of aluminum.

Tables 2 through 14 list the filter data for each of the fleet test vehicles. Filter residue deposits were rated qualitatively rather than quantitatively since attempts to completely separate the residues from the filters proved fruitless. Filters chosen for analysis samples were those which contained sufficient residue deposits for analysis.

2.2.2 Miscellaneous Samples

Miscellaneous samples acquired were predominantly in-line vehicle propane filter residues from DND vehicles not included in the fleet test controlled group. In total, over 300 DND vehicle filters were obtained. Filter residues from 2 propane powered buses were also obtained.

2.2.3 Compound Separation

Selected miscellaneous sample residues were mixed with ethanol, methanol, acetone and distilled water in order to separate any dissolvable compounds. Measured amounts of residues were mixed with 100 ml of each solvent and left for 24 hours. Mixtures were then filtered, and recovered residues were weighed. Recovered residue mass

TABLE 1 DND PROPANE VEHICLE TEST FLEET

DND Number	Make	Model	Engine	Tank*
84-71781	Chevrolet	Car	V6	SL.
84-74351	Dodge	Panel	318 V8	MA.
85-76686	Plymouth	Car	2.2 4 cyl.	MA.
85-77009	Clark	Tractor	4 cyl.	WO.
85-77047	Dodge	Van	318 V8	MA.
86-77762	Chev.	Pickup	350 V8	?
87-78288	Plymouth	Car	318 V8	MA.
87-79557	Dodge	Pickup	318 V8	MA.
87-79558	Dodge	Pickup	318 V8	MA.
87-80231	Chev.	Pickup	305 V8	SL.
87-80277	Chev.	Pickup	305 V8	SL.
88-82247	Plymouth	Mini Van	2.2 4 cyl	MA.
88-82249	Plymouth	Mini Van	2.2 4 cyl.	?

* Tank Manufacturers: SL. - Sleeger's, MA. - Manchester, WO. - Worthington (Aluminum).

TABLE 2 VEHICLE 84-71781 FILTER DATA

Last Change	Last Km	Prev. Km	Diff.	Deposits*	Sample#
	55951	46298	9653	H	1A
21/10/88	63252	60790	2462	M	
24/05/89	70751	68360	2391	S	

* H - heavy, M - moderate, S - slight, T - trace, N - none

TABLE 3 VEHICLE 84-74351 FILTER DATA

Last Change	Last Km	Prev. Km	Diff.	Deposits	Sample#
m	73446	59386	14060	H	2A
a	73446	59386	14060	S	
m21/10/88	76480	74618	1862	M	2B
a21/10/88	76480	74618	1862	T	
m19/12/88	83781	76480	7301	S	
a19/12/88	83781	76480	7301	S	
m28/06/89	84835	83781	1054	T	
a28/06/89	84835	83781	1054	N	
m06/09/89	85144	84835	309	T	
a06/09/89	85144	84835	309	N	

notes: m - main tank filter, a - auxiliary tank filter

TABLE 4 VEHICLE 84-76686 FILTER DATA

Last Change	Last Km	Prev. Km	Diff.	Deposits*	Sample#
	80821			S	3A
10/10/88	83910	81237	2673	S	3B
11/08/89	91112	90270	842	T	
06/09/89	91157	91112	45	T	
			6466	T	

* H - heavy, M - moderate, S - slight, T - trace, N - none

TABLE 5 VEHICLE 85-77009 FILTER DATA

Last Change	Last Km	Prev. Km	Diff.	Deposits	Sample#
17/10/88	1063	1035	28	N	
09/12/88	1082	1063	19	N	
06/01/89	1127	1082	45	N	
13/03/89	1164	1127	37	N	
19/07/89	1210	1164	46	N	

TABLE 6 VEHICLE 85-77047 FILTER DATA

Last Change	Last Km	Prev. Km	Diff.	Deposits*	Sample#
m			11950	M	5A
a			11950	S	5B
m19/10/88	98812	95779	3033	T	
a19/10/88	98812	95779	3033	T	

notes: m - main tank filter, a - auxiliary tank filter
* H - heavy, M - moderate, S - slight, T - trace, N - none

TABLE 7 VEHICLE 85-77762 FILTER DATA

Last Change	Last Km	Prev. Km	Diff.	Deposits	Sample#
			4077	M	6A
14/12/88	43892	39618	4274	S	
07/06/89	46532	43892	2640	S	
06/09/89		46532		T	

TABLE 8 VEHICLE 87-78288 FILTER DATA

Last Change	Last Km	Prev. Km	Diff.	Deposits	Sample#
	72477	49995	22482	S	7A
18/10/88	82831	78632	4199	S	
14/12/88	98389	82831	15558	T	
29/06/89	100494	98389	2105	N	

TABLE 9 VEHICLE 87-79557 FILTER DATA

Last Change	Last Km	Prev. Km	Diff.	Deposits*	Sample#
	7011	0	7011	H	8A
21/10/88	10014	9204	810	S	
10/12/88	12354	10014	2340	M	
19/04/89	14242	12354	1888	S	
27/06/89	14985	14242	743	T	

* H - heavy, M - moderate, S - slight, T - trace, N - none

TABLE 10 VEHICLE 87-79558 FILTER DATA

Last Change	Last Km	Prev. Km	Diff.	Deposits	Sample#
			3220	M	9A
18/10/88	11831	10889	942	M	
13/04/89	20041	13995	6046	T	
30/06/89	21131	20041	1090	T	

TABLE 11 VEHICLE 87-80231 FILTER DATA

Last Change	Last Km	Prev. Km	Diff.	Deposits	Sample#
	5094	0	5094	H	10A
17/10/88	9791	8787	1004	S	
12/07/89	19114	16048	3066	S	

TABLE 12 VEHICLE 87-80277 FILTER DATA

Last Change	Last Km	Prev. Km	Diff.	Deposits*	Sample#
			1751	S	11A
17/10/88	11184	9301	1883	S	
13/03/89	17385	13697	3688	S	
24/08/89	19578	17385	2093	S	

* H - heavy, M - moderate, S - slight, T - trace, N - none

TABLE 13 VEHICLE 87-82247 FILTER DATA

Last Change	Last Km	Prev. Km	Diff.	Deposits	Sample#
17/10/88	2635	696	1939	T	
	2962	2635	327	T	
16/12/88	7624	2962	4662	T	
29/05/89	7958	7624	334	T	
11/08/89	14493	8354	6139	T	12A
			730	T	

TABLE 14 VEHICLE 87-82249 FILTER DATA

Last Change	Last Km	Prev. Km	Diff.	Deposits*	Sample#
17/10/88	1991	248	1743	T	
23/11/88	7311	1991	5320	T	
14/01/89	26424	7311	19113	T	
29/06/89	37189	26424	10765	S	
11/09/89	53156	37189	15967	T	
	72221	53156	19065	S	13A

* H - heavy, M - moderate, S - slight, T - trace, N - none

was then subtracted from initial residue mass, to give the amount dissolved. Mass was measured to .001 g.

2.2.4 Scanning Electron Microscopy

Each DND fleet test residue sample, and selected miscellaneous samples, were placed in a scanning electron microscope (SEM) for observation. Residue appearance, texture and particulate size were observed and compared for each sample.

2.2.5 Energy Dispersive Spectroscopy

All samples placed in the SEM and subjected to a high energy electron beam produced x-ray emissions, characteristic of the elements present. The characteristic x-rays were collected and analyzed by energy dispersive spectroscopy (EDS) to give a quantitative elemental analysis for each sample. Elements lighter than sodium, however, could not be quantified or detected due to the absorption characteristics of the x-ray detector window used.

2.2.6 X-Ray Diffraction Analysis

All fleet test samples, and selected miscellaneous samples, were analyzed using x-ray diffraction for identification of the crystalline compounds and phases present.

All fleet test samples were analyzed using a Philips PW1710 Diffractometer with Cu radiation and a single crystal monochromator. Residues were ground to a fine powder in an agate mortar, mixed with acetone, and smeared on amorphous glass slides. Slides were then

loaded into the diffractometer, and patterns were acquired from 10 to 100 degrees of 2θ, at 6 degrees per minute scan speed.

Selected miscellaneous samples which contained large amounts of residue were analyzed in a Philips PW1130/60 diffractometer using Cr radiation with a Vanadium Kβ filter. Residues were ground into fine powders and packed into the window of an aluminum sample holder. Samples were then loaded into the diffractometer and patterns collected from 25 to 140 degrees of 2θ, at 1/2 degree per minute scan speed.

2.3 Decommissioned Propane Vehicle Tank Analysis

2.3.1 Tank History

The full manufacturer's build data for the decommissioned tank was obtained from Manchester Tank Canada Ltd. by tracing the serial number of the tank. The tank was designed for a Dodge Pickup truck application, and was built in March 1983. Tank shell and heads were both constructed from ASTM 414G pressure vessel grade steel (Hot rolled plate steel, .31% C - 1.35% Mn - .035% P - .04% S, used in the as-rolled condition[27]).

The tank was installed in a 1982 Dodge 1 ton 4X4, and was removed after 42186 km, which corresponded to 5600 litres of propane. During its service, the tank produced sufficient black magnetic residue to require 25 filter changes, and 2 mixer (propane carburetor) replacements, because of residue contamination.

2.3.2 Tank Specimen Preparation

The entire tank was sawed in half across the center of the shell, and small tank wall sections were then cut out for analysis.

For XRD analysis of the tank wall surfaces, 5 mm by 20 mm samples were cut from the tank shell and end cap. For analysis of the outside tank surface, acetone was used to remove the 2 layers of paint.

All tank wall section samples for SEM analysis and optical microscopy were carefully wrapped in aluminum or stainless steel foil, cut on a diamond wheel cutter at low speed, and mounted in bakelite at low temperature in order to preserve the integrity of the oxide layer.

Samples were rough ground on SiC paper to 600 grit, then

polished to .25 μm with diamond paste on lapping wheels. Selected samples were also etched in 2% nital, or 1% HCl in alcohol, to reveal the microstructure of the tank wall steel, or oxide layer, respectively.

Small sections of the 80% outage gauge dip tube and liquid withdrawal tube found within the propane tank were also cut out, and samples were prepared for SEM and optical analysis by the methods described above.

A yellow painted steel grade specification marking was discovered stenciled on the inner surface of the tank shell. Two independent sections of the specification marking were carefully cut out, and samples prepared for SEM and Optical analysis by the previously mentioned techniques.

2.3.3 Optical Analysis

Tank wall, liquid withdrawal tube and dip tube sections were observed under a Nikon microscope at 400 and 1000X magnification. The presence and/or thickness of any oxide layers present were recorded. In the etched samples, the microstructures of the base metals were observed and compared to that of the specified materials.

The specification marking sections were observed at 1000X magnification to study the relationship between substrate metal, oxide layer and specification marking.

2.3.4 SEM Analysis

All tank samples were observed in a scanning electron microscope at magnifications up to 3000X. Secondary electron images were used to study the specification marking sections, the oxide layers present on the tank wall sections, and to search for evidence of oxide layers on the liquid withdrawal tube and dip tube sections.

SEM back scattered electron images were also used to study the composition of the tank wall oxide layer(s). In compositional back scattered images, different phases are revealed in contrasting brightness.

Additional small samples of the tank wall were cut from the tank, and placed directly in the SEM to observe the oxide layer(s) topographically.

EDS was used to analyze the composition of the tank wall base metal, liquid withdrawal tube, dip tube, specification marking and any oxide layers present.

2.3.5 X-Ray Diffraction Analysis

XRD sample sections cut from the tank shell and end caps were placed directly in the diffractometers so the surface layers could be analyzed in an undisturbed state. Both PW1710 and PW1130/60 diffractometers were used with monochromatic Cu Kα radiation, and vanadium filtered Cr Kα radiation, respectively. Oxide layers from both the inside and outside of the tank were analyzed and compared.

CHAPTER 3 RESULTS

3.1 Particulate Residue Analysis Results

3.1.1 Compound Separation Results

Filter residues from DND vehicles 84-71833 and 88-82118 were mixed with ethanol, methanol, acetone and distilled water. Residues from these vehicles are considered to be typical of the residues in the controlled group. No mass loss could be measured, indicating the residues were completely insoluble in each solvent.

3.1.2 SEM Analysis Results

Each of the DND fleet test residues, along with selected miscellaneous residue samples, were observed in a Scanning Electron Microscope. All residues were found to be similar in appearance. Residues were predominantly thin flakes as shown in Figure 2 and Figure 3. Flakes were typically 7 to 12 μm thick as shown in Figure 4. Some residue samples contained a few small hollow spheres, as shown in Figure 5, and other small ($<10\mu m$) miscellaneous particles. Most residues also contained a small amount of fibres from the in-line

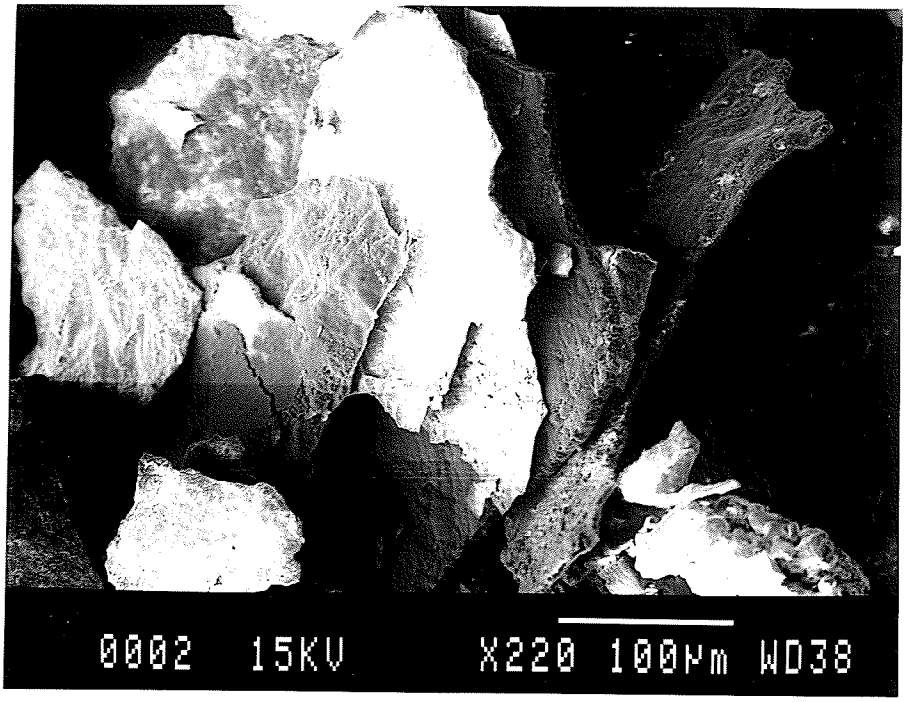

FIGURE 2 Residue Flakes 1

FIGURE 3 Residue Flakes 2

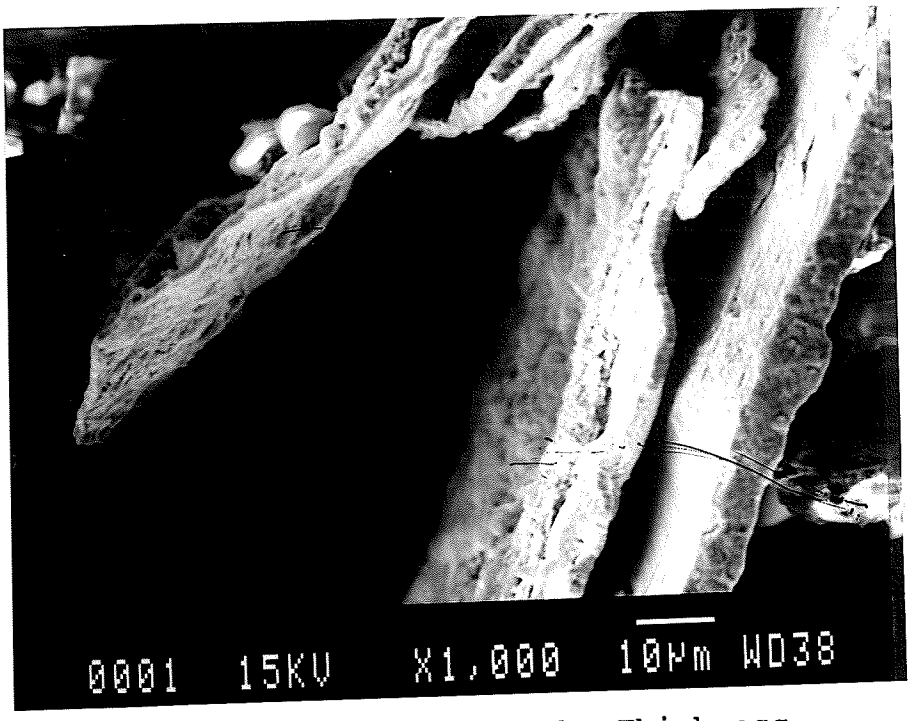

FIGURE 4 Residue Flake Thickness

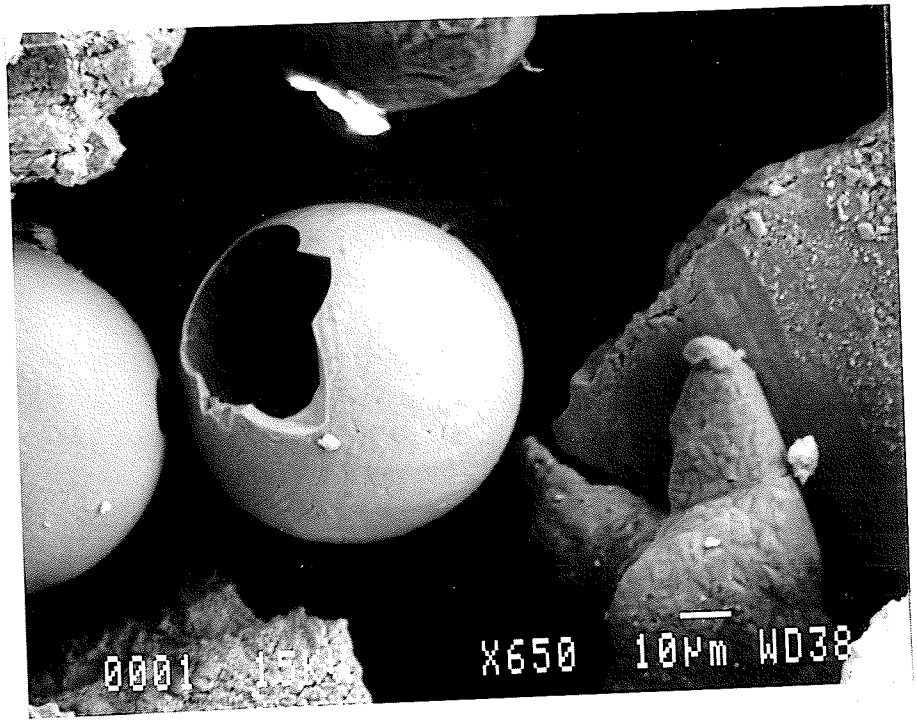

FIGURE 5 Hollow Iron Spheres

propane filters.

3.1.3 EDS Analysis Results

Table 15 lists the EDS analysis results for the residues from the DND fleet test. Table 16 gives EDS results for miscellaneous residue samples. Controlled group residues were predominantly iron, with typically only traces of other elements present. Miscellaneous residue analysis results were similar, except for the bus residues which contained more impurities.

The 2 different types of in-line filters used in the DND vehicles were also analyzed. Results are listed in Table 15.

3.1.4 XRD Analysis Results

Table 17 lists the compounds identified by x-ray diffraction for the DND fleet test residues, and for 3 miscellaneous residues. Figure 6 shows a typical diffractogram from the PW1710 diffractometer. All residues were found to be primarily common oxides of iron, except for the residue from bus 116, which

TABLE 15 EDS ANALYSIS FOR DND TEST FLEET RESIDUES
(atomic % average of 3 acquisitions)

filter #	vehicle #	Fe	Mn	Si	S	Al	Ca	K	Ti	Cr	Cl	Cu	Na	Zn	Mg
1A	84-71781	95.5	1.41	0.98	1.23	0.61	0.33	0.12	0.12						
2A	84-74351	93.8	1.35	2.11	1.65	0.30	0.17	0.19		0.21	0.18				
2B	84-74351	89.1	1.32	3.38	1.17	3.74	0.45	0.30		0.19	0.35				
3A	85-76686	88.1	1.10	3.78	3.55	1.76	0.40			0.38	0.31	0.63			
4A	85-77009	no residue found													
5A	85-77047	82.9	1.20	4.45	0.97	8.93	0.54		0.9	0.10	0.26				
5B	85-77047	59.7	0.76	10.5	11.50	14.80	0.85					2.30			
6A	86-77762	95.3	1.02	1.87	1.10	0.31	0.39		0.04						
7A	87-78288	59.8	0.91	7.37	2.21	28.90	0.84								
8A	87-79557	85.0	0.96	1.57	0.61	6.22	0.72		0.28		0.32		4.42		
9A	87-79558	56.2	0.99	2.72	1.04	35.70	0.39	0.09	0.06		0.13		2.70		
10A	87-80231	83.9	0.93	3.10	0.99	6.27	0.58	0.46	0.48		0.52	1.36	0.67	0.78	
11A	87-80277	83.7	0.80	8.11	1.74	3.62	2.03				0.88				
12A	88-82247	not enough residue for analysis													
13A	88-82249	43.5	0.17	12.00	25.50	8.40	0.81	0.13				8.76		0.91	
FILTER 1	MATERIAL	1.8		8.89	2.53	55.80	0.85		1.37		10.78		10.03	4.10	3.88
FILTER 2	MATERIAL	30.8	0.65	9.64	29.10	19.40	1.19	0.38				3.78	2.81	2.29	

TABLE 16 EDS ANALYSIS OF MISCELLANEOUS RESIDUES
(atomic %)

sample	Fe	Mn	Si	S	Al	Ca	K	Ti	Cr	Cl	Cu	Na	Zn	Mg	P
88-82117	94.6	2.88	2.51												
A14b	59.7	0.76	10.52	11.05	14.82	0.85					2.70				
A30	95.0	1.19	0.91	1.72	1.22										
87-79574	51.5	1.29	3.19	2.01	38.30	0.58					1.77		1.36		
88-82815	89.7	1.77	1.76			0.37						6.36			
85-79341	90.0	1.34	2.59	1.76	2.09	0.29					1.91				
84-74353	86.9	2.71	7.13	1.05		0.51								1.71	
85-77088	90.4	1.32	1.71	0.27	5.49					0.76					
Bus 116	67.6	0.85				0.99									30.58
Bus S	84.6	0.80	2.89	1.68	8.85	0.89		0.27							

TABLE 17 X-RAY DIFFRACTION COMPOUND ANALYSIS

Sample	Identified Compounds
DND Fleet Test Residues	
1A	Fe_3O_4, αFe_2O_3, FeO, (p) Mn_3O_4
2A	Fe_3O_4, αFe_2O_3, FeO, Fe, SiO_2, (t) γFeO(OH)
2B	Fe_3O_4, αFe_2O_3, FeO, Fe, SiO_2
3A	Fe_3O_4, αFe_2O_3, FeO, Fe, SiO_2, (t) γFeO(OH), (p) $Fe_2(SO_4)_3$
4A	No deposits found
5A	Not enough deposits for x-ray analysis
5B	Fe_3O_4, αFe_2O_3, FeO, Fe, SiO_2, Al, (p) $Ca_2Al_2SiO_7$, (p) Cu_2O
6A	Fe_3O_4, αFe_2O_3, FeO, Fe, SiO_2
7A	Fe_3O_4, αFe_2O_3, FeO, Fe, SiO_2, Al
8A	Fe_3O_4, αFe_2O_3, FeO, Fe, SiO_2, Al
9A	Fe_3O_4, αFe_2O_3, FeO, Fe, Al, (p) Fe_3C
10A	Fe_3O_4, αFe_2O_3, Fe, Al
11A	Not enough deposits for x-ray analysis
12A	Not enough deposits for x-ray analysis
13A	Fe_3O_4, αFe_2O_3, Fe, Al, SiO_2, (p) $Ca_2Al_2SiO_7$, (p) Cu_2O
Miscellaneous Residues	
A30	Fe_3O_4, (t) αFe_2O_3, (t) FeO
Bus 116	Fe_3O_4
Bus S	Fe_3O_4, αFe_2O_3, FeO, Fe

notes: (t) - trace, (p) - possible

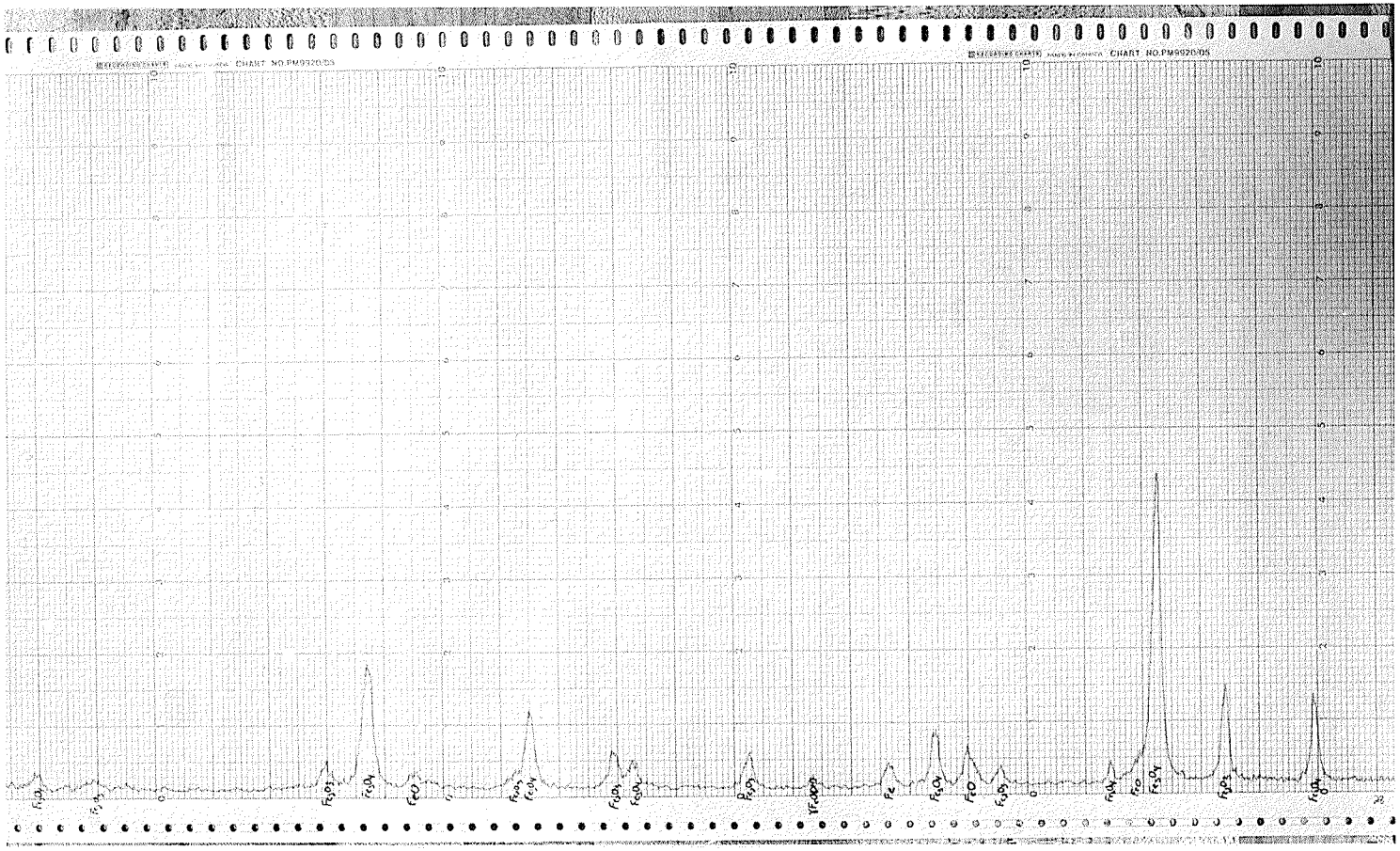

FIGURE 6 X-Ray Diffractogram of DND Sample 2A

contained other impurities.

3.2 Propane Tank Analysis Results

3.2.1 Optical Analysis Results

Etched tank wall sections were found to have a microstructure consistent with the specified ASTM 414G steel. Figure 7 shows the tank shell microstructure, and Figure 8 shows that of the tank end cap.

Etched sectioned of the liquid withdrawal tube and 80% outage gauge dip tube, contained within the tank, both showed a microstructure corresponding to very low carbon steel. Figure 9 and Figure 10 show the microstructures of the dip tube and withdrawal tube, respectively.

Both the liquid withdrawal tube and dip tube showed no evidence of oxide layers at 1000X magnification. Figure 11 and Figure 12 show the outer edges of the withdrawal tube and dip tube, respectively. No oxide layer can be seen between the aluminum protective wrap and the base metal.

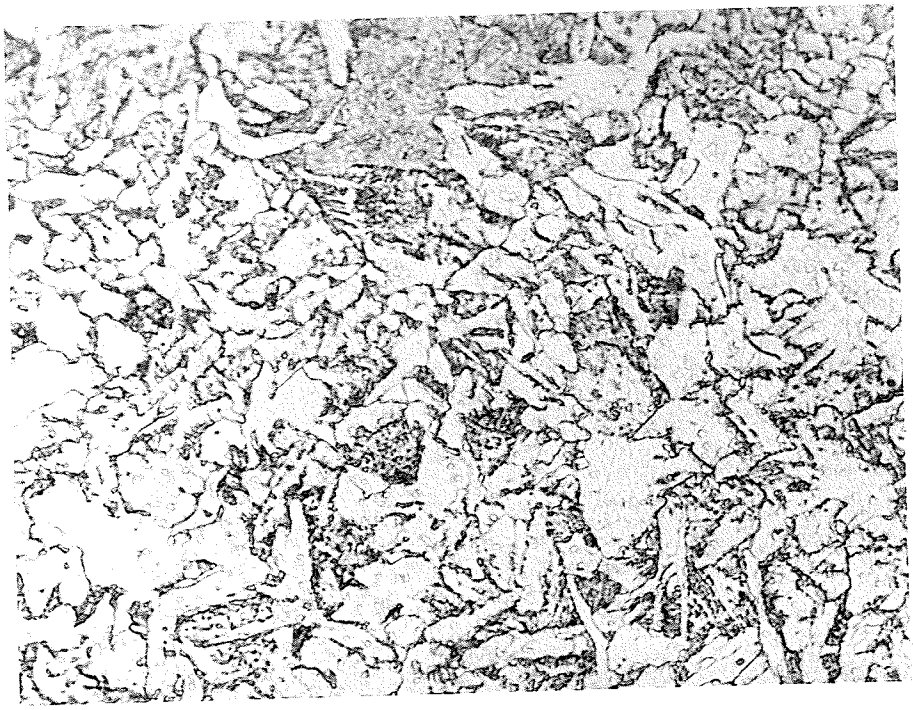

FIGURE 7 Tank Shell Micro Structure (1322X)

FIGURE 8 Tank End Cap Micro Structure (1322X)

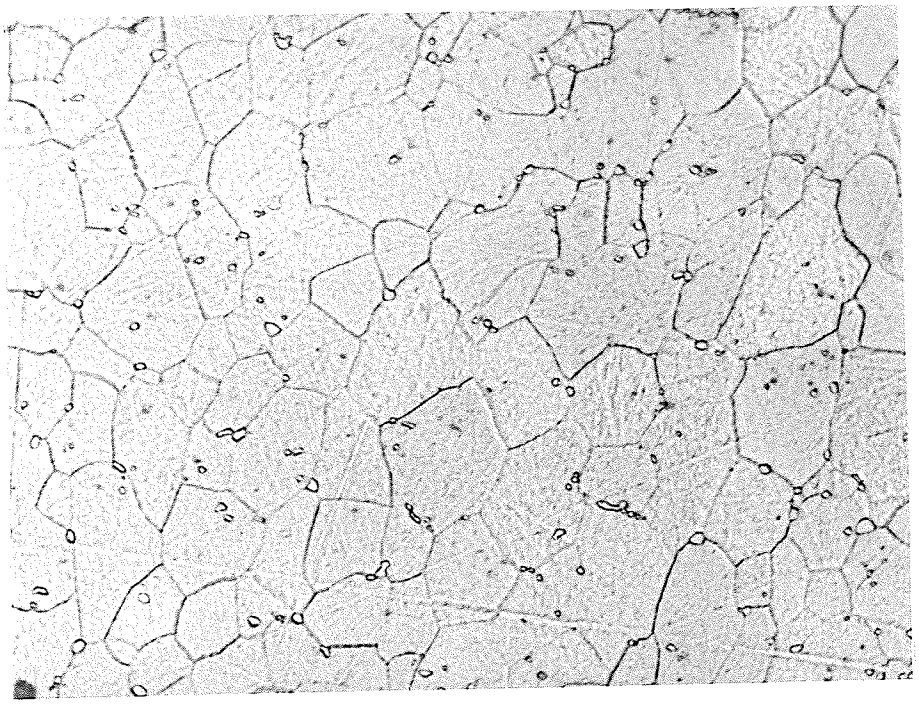

FIGURE 9 Dip Tube Micro Structure (1322X)

FIGURE 10 Liquid Withdrawal Tube Micro Structure (1322X)

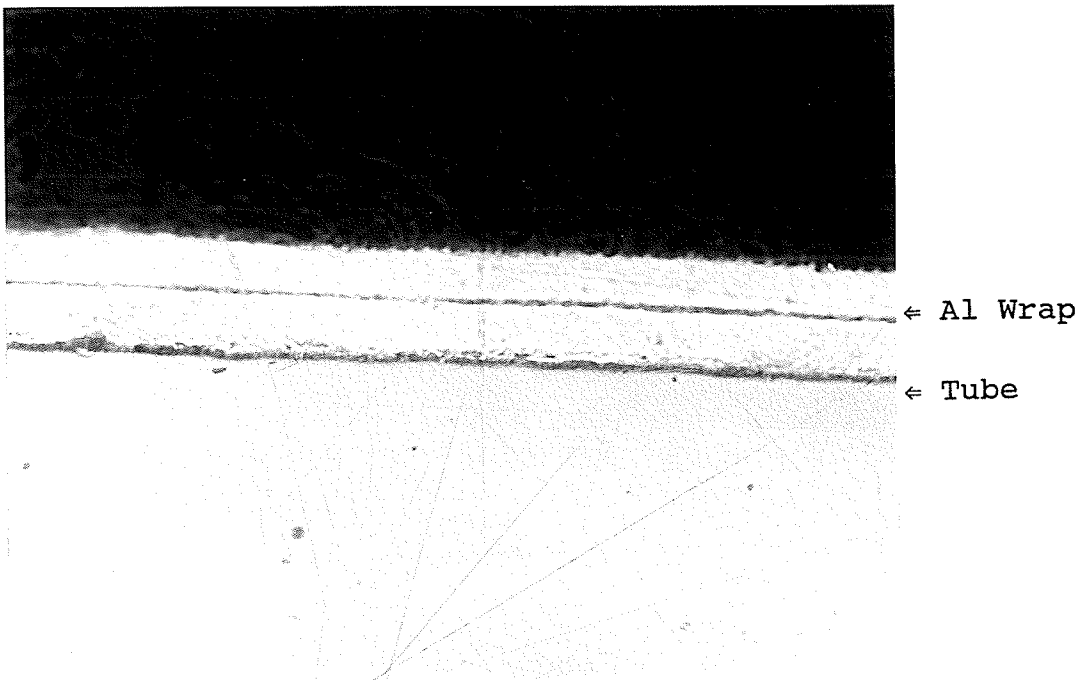

FIGURE 11 Edge of Liquid Withdrawal Tube (535X)

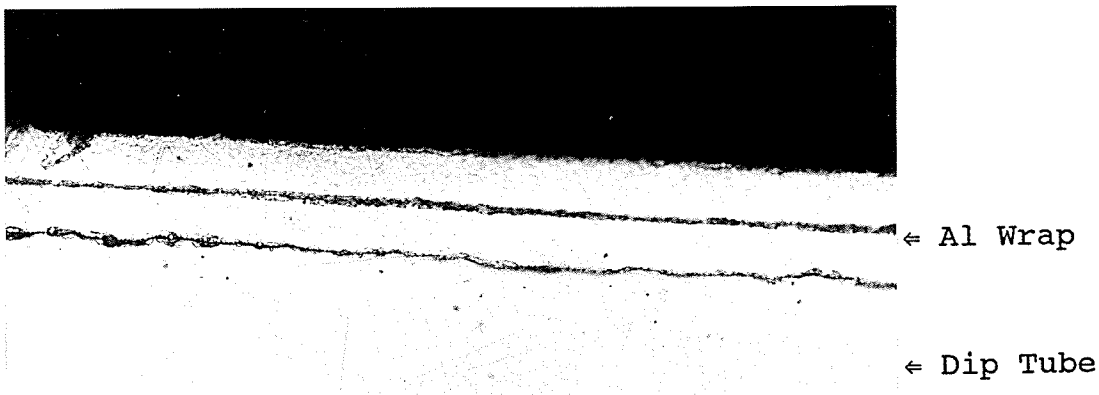

FIGURE 12 Edge of Dip Tube (535X)

The tank wall sections, however, showed a significant oxide layer. Figure 13 shows a 10 μm thick oxide layer on the inner surface of the tank shell. Figure 14 shows a similar oxide layer under the factory paint on the outside surface of the tank shell. Similar oxide layers were found on the surfaces of the tank end caps. Figure 15 shows the 10 μm oxide layer under the paint on the outside surface of one end cap.

Optical analysis of the specification marking showed the paint marking was applied over the oxide layer. That is, the sequence of layers is:

base metal - oxide layer(s) - specification marking.

Figure 16 and Figure 17 show the paint marking on the outside of a uniform thickness oxide layer, from 2 independent sections of the tank shell.

Etched oxide layer sections failed to show the presence of more than one layer of oxide.

3.2.2 SEM Analysis Results

Tank wall oxide layers were observed in the SEM using both secondary electron images (SEI), and back scattered electron images for compositional analysis. SEI

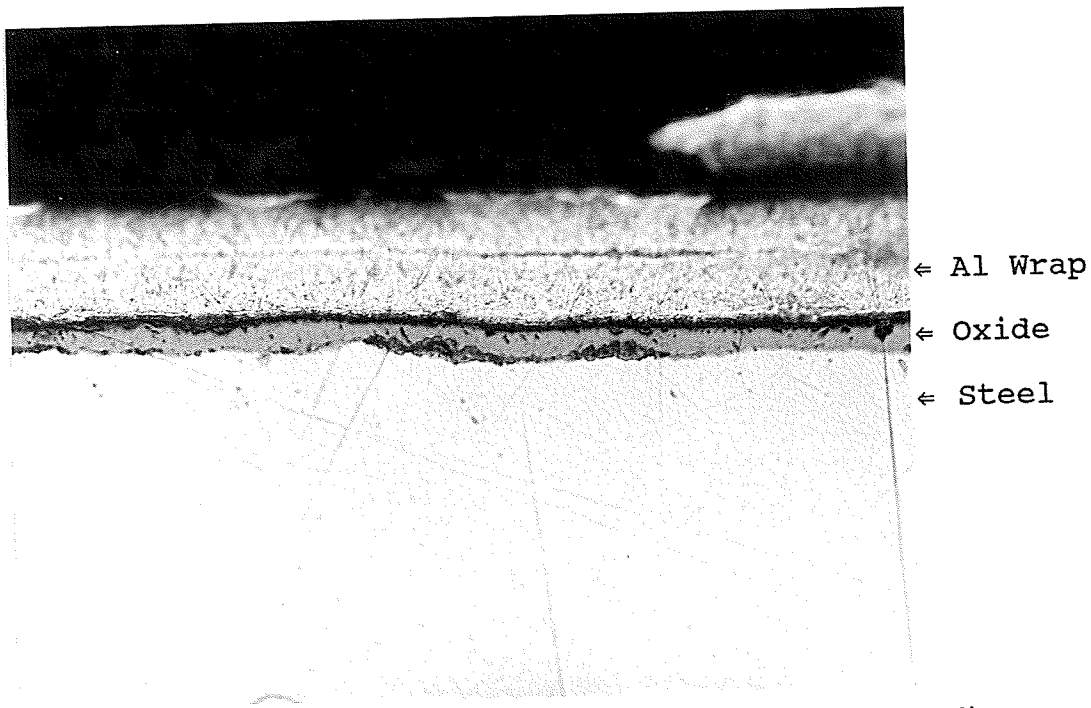

FIGURE 13 Interior Tank Shell Oxide Layer (535X)

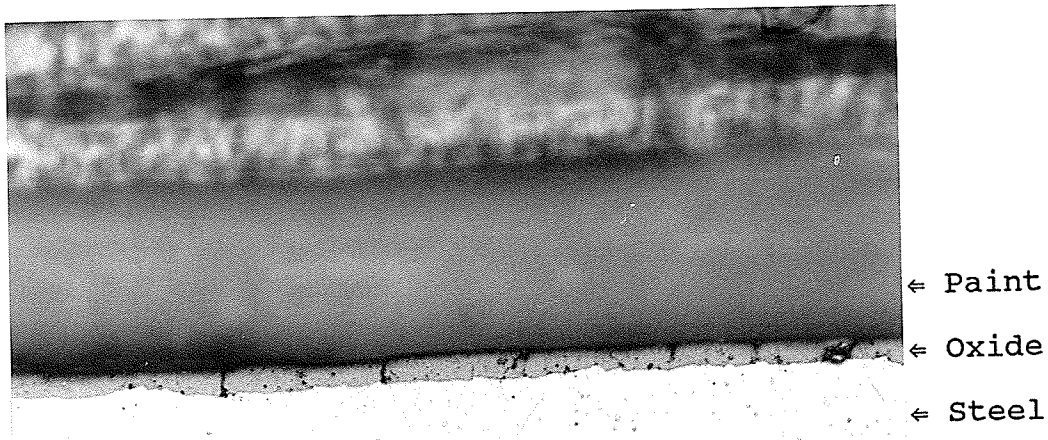

FIGURE 14 Exterior Tank Shell Oxide Layer (535X)

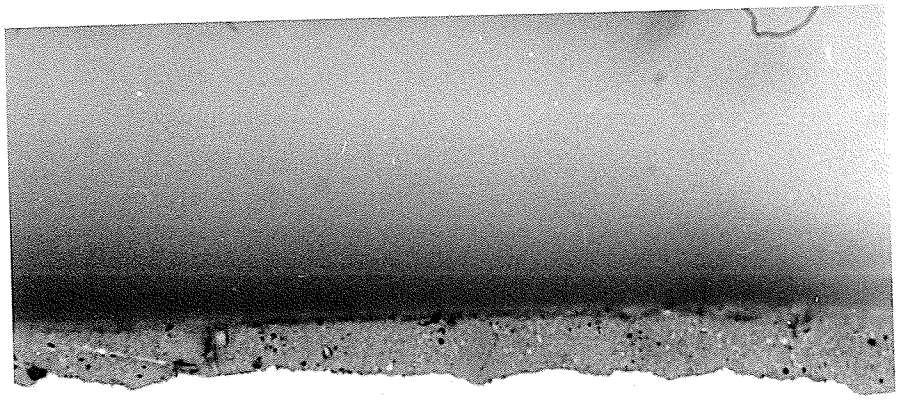

FIGURE 15 Exterior Tank End Cap Oxide Layer (1322X)

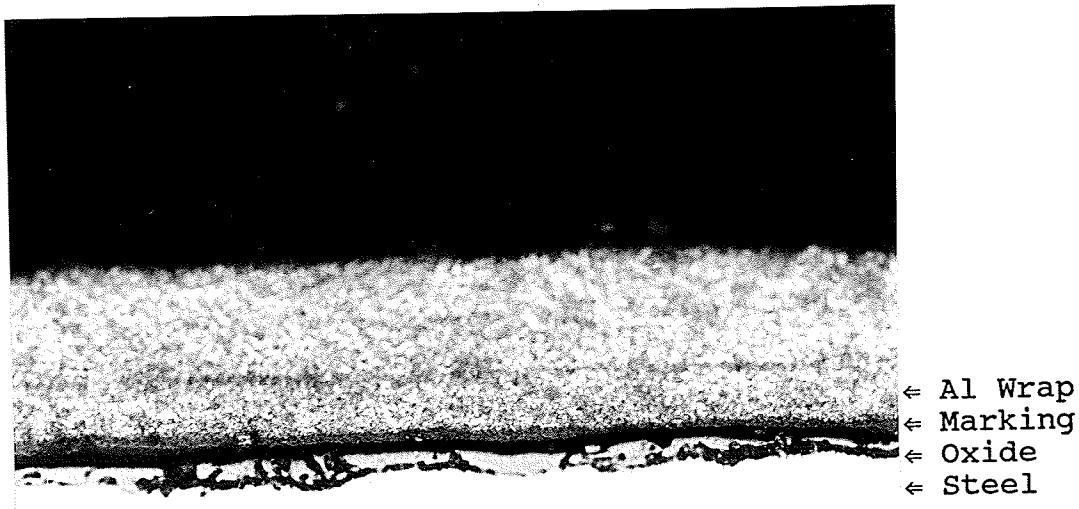

FIGURE 16 Specification Marking 1 (optical 535X)

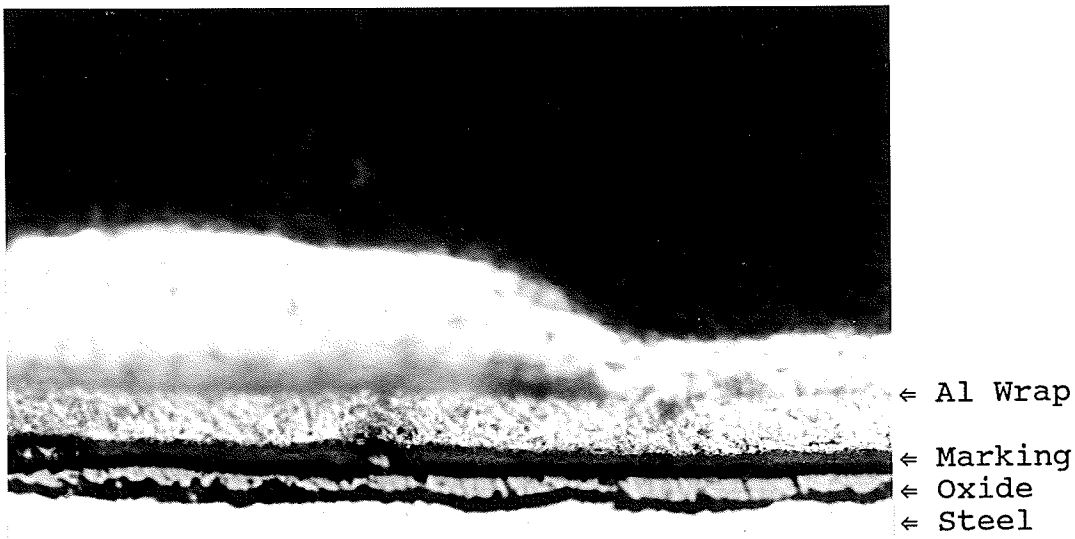

FIGURE 17 Specification Marking 2 (optical 535X)

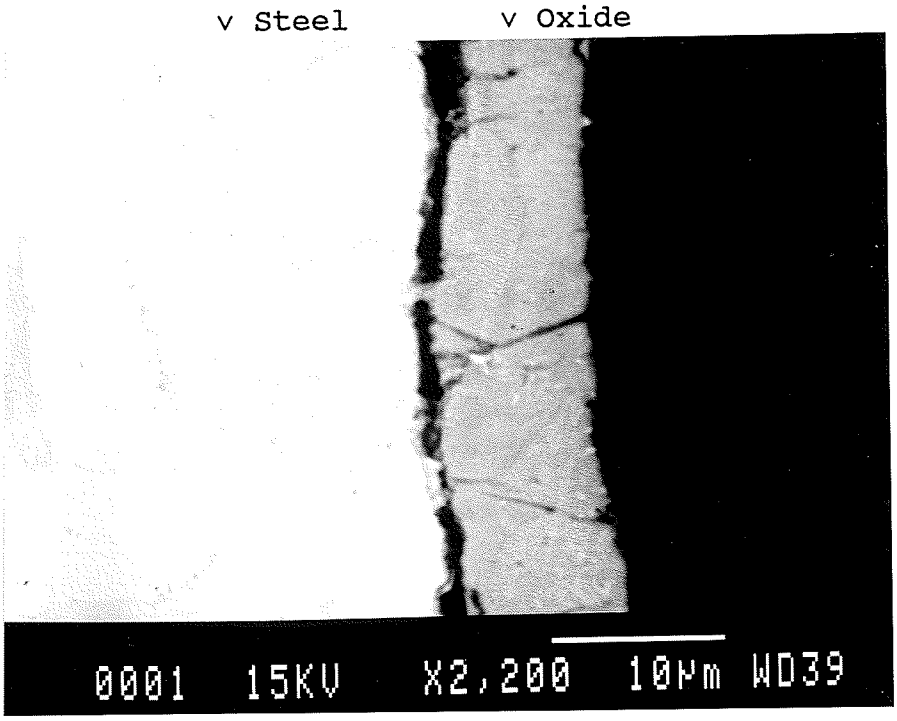

FIGURE 18 Oxide Composition (Back-scattered Electrons)

showed a uniform oxide layer on both surfaces of the tank shell and end caps, of 10 μm nominal thickness. The interior oxide layer showed signs of stress cracking and loss of adhesion, while the exterior oxide layer appeared more adherent and continuous.

Compositional analysis of the oxide layer using back scattered electrons showed the oxide layer to be a predominantly uniform singular phase. Figure 18 shows the interior tank shell oxide layer using compositional mode back scattered electrons.

Tank wall specification mark sections observed using secondary electron images showed a uniform thickness oxide layer under the specification marking. Oxide layer appearance and thickness under the specification marking was identical to the appearance and thickness elsewhere. Figure 19 shows the specification marking (cross hairs) between the oxide layer and the protective aluminum wrap. Figure 20 and Figure 21 show the specification marking from a different section.

Secondary electron images were also used to directly observe the surfaces of the tank oxide layers. Outside tank oxide surfaces were observed after carefully removing the factory paint with acetone. Evidence of

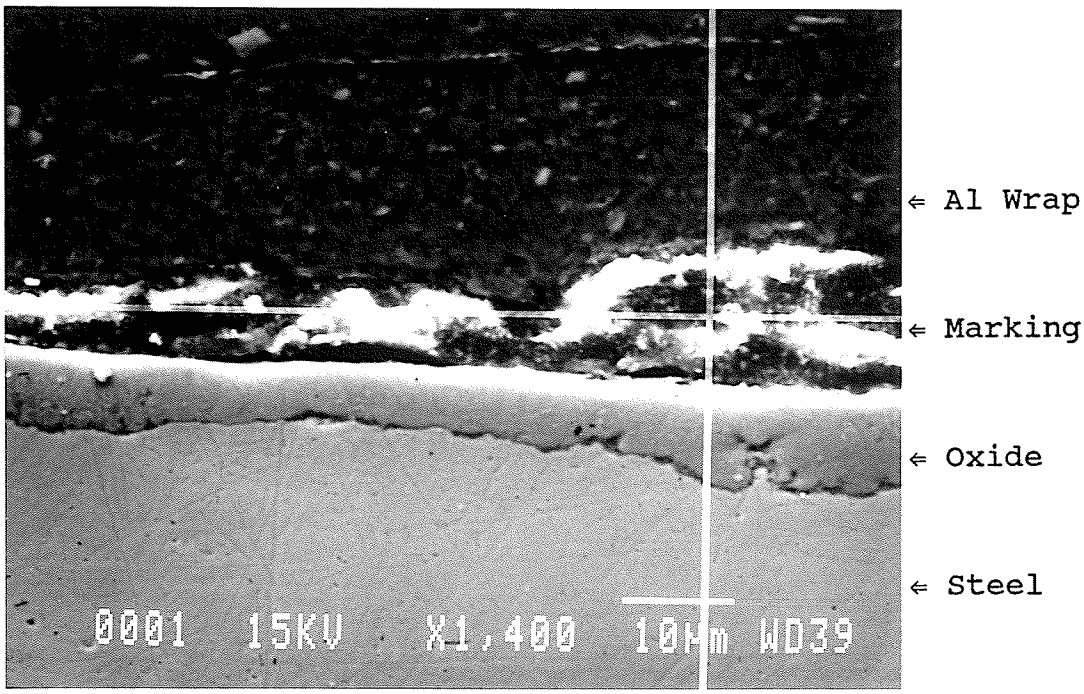

FIGURE 19 Specification Marking 1 (SEM)

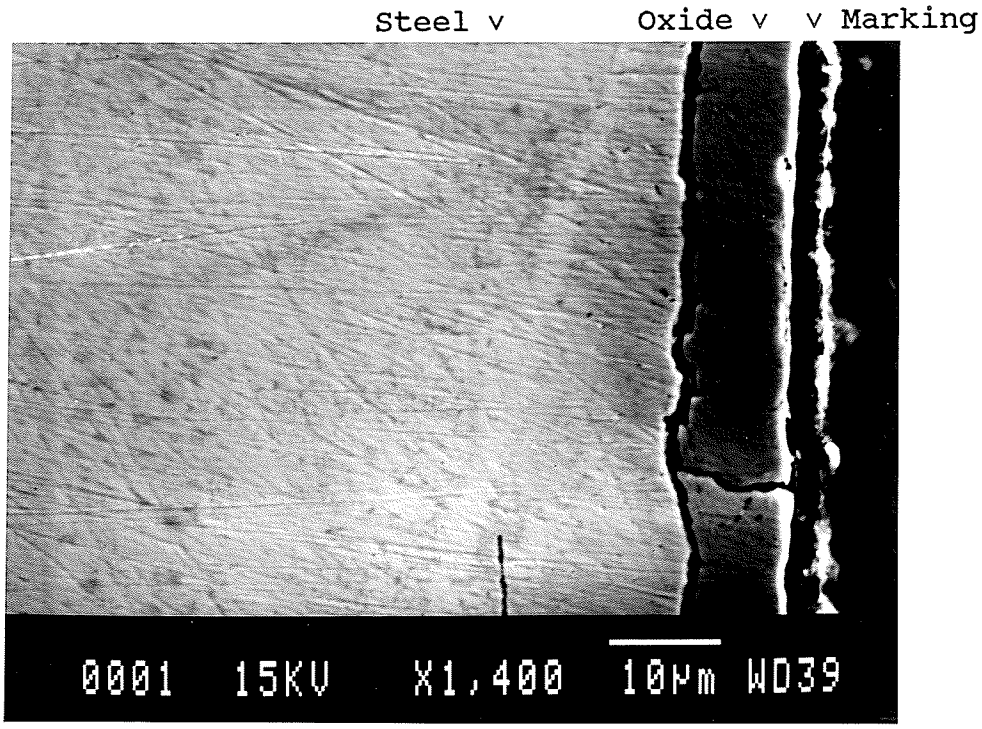

FIGURE 20 Specification Marking 2 (SEM)

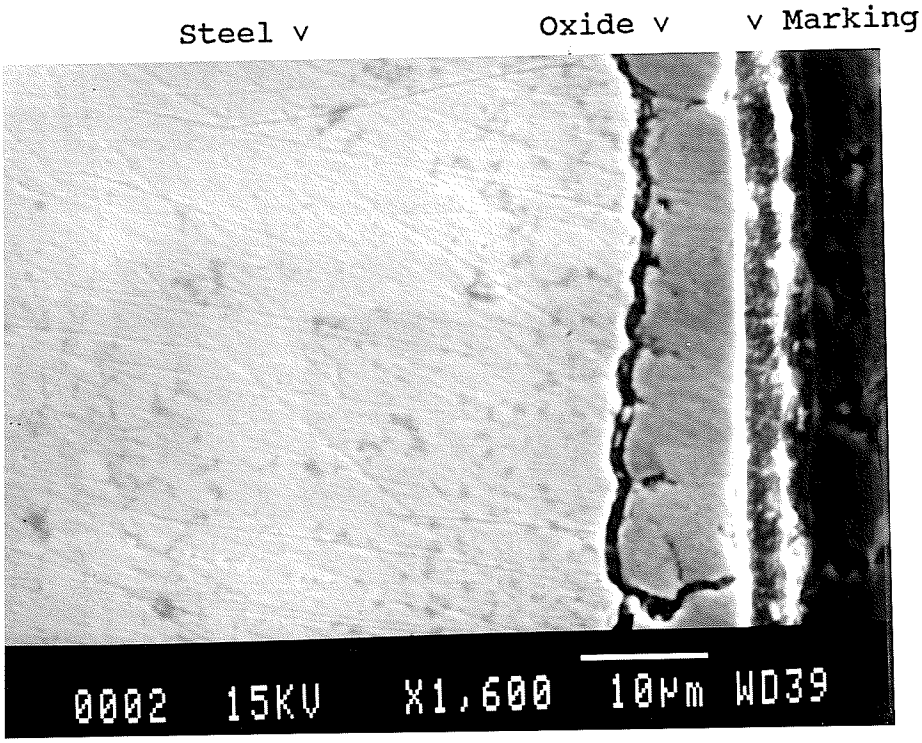

FIGURE 21 Specification Marking 3 (SEM)

FIGURE 22 Interior Oxide Layer Spallation (1100X)

oxide spallation was clearly observed on the inside oxide of the tank shell. The surface showed a large number of small areas where the oxide had spalled off, and numerous stress cracks. Figure 22 shows parts of the inner oxide layer which have partially lost adhesion, adjacent to a spalled area. The outside tank shell oxide surface showed little evidence of spallation, although stress cracks were found. Both tank end cap oxide surfaces showed little evidence of oxide spallation, but stress cracks were observed.

SEM analysis of the liquid withdrawal tube and dip tube showed no evidence of oxide layers at up to 3000X magnification. Figure 23 shows the outside edge of the liquid withdrawal tube. No oxide is visible between the tube and protective aluminum wrap.

EDS chemical analysis was performed on the liquid withdrawal tube, dip tube, tank wall, oxide layer and specification marking. Table 18 gives the elemental composition results from the EDS. As expected, the liquid withdrawal tube and dip tube had a low carbon steel composition, the tank wall composition corresponded to ASTM 414G specifications, the oxide layer contained only traces of elements other than iron, and the specification marking had the composition of paint.

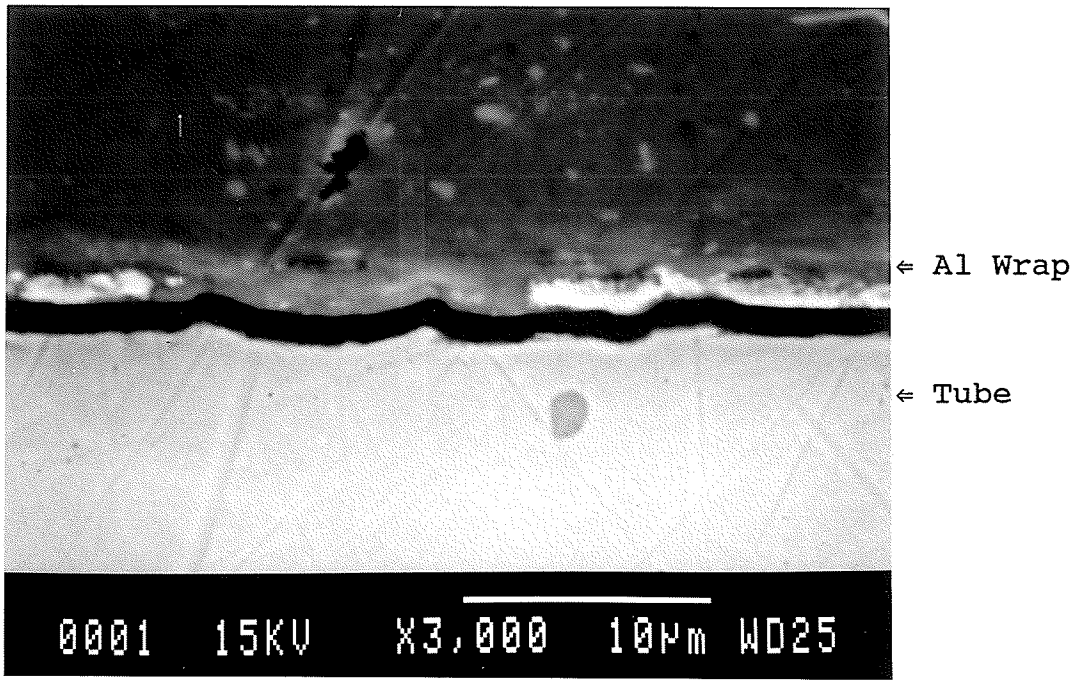

FIGURE 23 Edge Of Liquid Withdrawal Tube (SEM)

3.2.3 XRD Analysis Results

Sections of the tank shell and end caps were placed directly in the diffractometers to analyze the composition of the oxide layer(s). The composition was found to be Fe_3O_4, with only traces of αFe_2O_3 and FeO. Figure 24 shows the XDR PW1710 diffractogram of the tank shell interior oxide layer. Oxide layer composition was found to be consistent from tank shell to end cap, and from tank interior to tank exterior.

TABLE 18 EDS ANALYSIS OF TANK COMPONENTS
(weight % average)

component	Fe	Mn	Si	S	Al	Ca	K	Ti	Cr	Cl	Cu	Na	Zn	Mg
Spec. Marking	5.89	0.15	15.6	1.61	16.6	0.66	0.7	54.9		3.81				
Tank Shell	97.6	1.56	0.83											
Tank End Cap	97.6	1.53	0.86											
Fill Tube	99.3	0.45	0.2											
Vent Tube	99.1	0.61	0.24											
Tank Oxide	97.9	1.38	0.44											

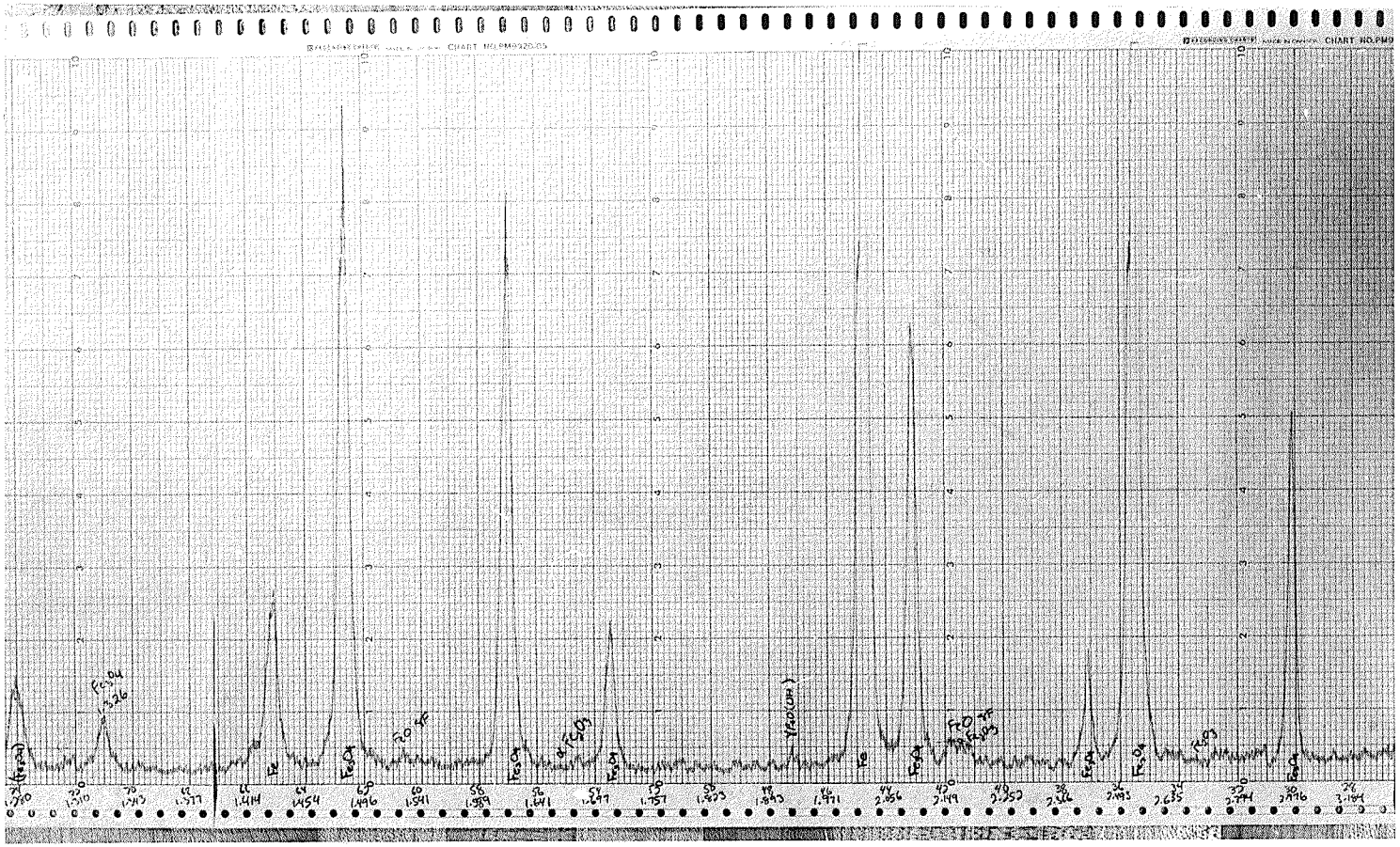

FIGURE 24 X-Ray Diffractogram of Tank Oxide Layer

CHAPTER 4 DISCUSSION

4.1 Particulate Residues

Since compound separation attempts failed to dissolve any measurable amount of residue, the residues can not contain any significant amount of organics from the propane. The residues then, must be predominantly stable insoluble inorganics, minerals and oxides.

Results from XRD and EDS analyses (Tables 15-17) show the residues to be primarily common oxides of iron. Magnetite, Fe_3O_4, was the predominant compound in all residues. Other compounds were typically identified in only trace amounts in the controlled group residues.

Metallic iron found in the residues is likely due to weld splatter from the tank manufacturing process, as are the hollow iron based spheres shown in Figure 5. Traces of SiO_2, $Ca_2Al_2SiO_7$ and metallic Al detected in the residues, can be attributed to weld slag[2] from the tank itself, or tiny shavings from the aluminum tank float gages, respectively. Other contaminants detected in trace amounts were most likely particles less than 10 μm which originated in the propane distribution system, and passed

through the early incident filters during propane filling of the test fleet tanks. EDS analysis of the bus residues clearly illustrates the amount of contaminants which can be present in the propane distribution system, since the buses were not filled under controlled conditions with filtered propane.

The significant amounts of sulfur found in some samples likely came from a molecular sieve (which trap some sulfur compounds in the propane distribution system[12]) which occasionally rupture. Since a molecular sieve is constructed of a sodium-aluminum-silicate compound, zeolite, the presence of these elements in the residues could also be due to a molecular sieve failure.

Many of the residue samples used for EDS analysis also contained significant amounts of filter fibres, due to the difficulty of separating the residues from the filters. Comparison of the EDS analyses of the filters, with those of the residues, can also account for the presence of some elements in the residues.

Selected bag filters, which were used to filter the propane on introduction to the test fleet tanks, were examined and found to be free of large amounts of the characteristic black magnetic residues found in the

vehicle filters, indicating no large amount of black residue exists in the propane distribution system. During the DND test, no incident bag filter ever failed. Since all propane was filtered to at least 10 μm on introduction to the test fleet propane tanks, any residue particle greater than 10 μm in the controlled group residues must have originated in the tank itself. Therefore, the large black oxide flakes found in the residues, as shown in Figures 2 and 3, which were found to exceed 1 mm in some samples, must have originated in the vehicle tanks.

4.2 TANK ANALYSIS

Metallographic examination and EDS analysis of the tank shell, end caps, outage gage dip tube, and liquid withdrawal tube showed no metallurgical inconsistencies, indicating the manufacture of the tank and inner structures met all construction specifications.

Optical and SEM examination of the tank shell and end cap sections showed an interior oxide layer of 10 μm nominal thickness. EDS and XRD analysis of the oxide layer showed the oxide layer to have a composition corresponding exactly to that of the black magnetic oxide flakes found

in the vehicle filter residues. Comparison of XRD diffractograms of the residues and tank wall, Figures 6 and 24, respectively, clearly shows the compositional match. It can therefore be concluded that the black magnetic residues are simply flakes of tank wall oxide, which have spalled off. This conclusion is supported by the fact that the one aluminum tank in the DND test fleet failed to produce any black magnetic residue, and by Figure 22 which shows spallation of the interior tank shell oxide layer.

4.3 THE TANK OXIDE LAYER

Since spallation of the interior tank wall oxide is the cause for the black magnetic residues, the origin of the interior tank oxide will now be considered. There are 2 possibilities: 1. Formation in the tank during service, by reaction with the propane or impurities contained within, or 2. Formation during the manufacture of the tank, or the steel plate itself.

4.3.1 Oxide Formation During Tank Service

It will be proven that oxide formation during tank

service is not reasonably possible. The reader is first referred to the Appendix for a brief summary of the theory of oxidation of steel.

Since analysis of the interior tank oxide showed the layer to be composed of magnetite with only traces of hematite and wüstite, consideration will be given to the growth of a magnetite layer only. Parameters from the studied decommissioned tank will be used:

final oxide thickness - 10 μm

total service time - 3.5 years

maximum service temperature - 37°C

Calculations will first be made assuming the tank had no oxide layer present at the start of service, and sufficient oxygen was present so that the outward diffusion of iron ions is the rate controlling step of oxidation. The growth of the magnetite layer will therefore follow parabolic kinetics, and the oxide weight gain per unit surface area, w, is described by:

$$w = k_p \sqrt{t} \qquad - 1$$

where k_p is the parabolic rate constant, and t is time. Oxide thickness can be converted to weight gain per unit area by:

$$w = \frac{3\xi m_o \rho_{ox}}{m_{ox}} \qquad - 2$$

where m_{ox} is the molecular weight of the oxide (232g/mole

for magnetite), ρ_{ox} is the density of the oxide (5.2 g/cm^3 for magnetite[3]), ξ is the oxide thickness, and m_o is the atomic weight of oxygen (16g/mole). From Eq 1 and Eq 2, a 10 μm thick magnetite layer grown in 3.5 years will then require a parabolic rate constant of $7.932 \times 10^{-7} g/cm^3 min^{-1/2}$.

The parabolic rate constant is given by:

$$k_p = k_o \exp\left(\frac{-Q}{RT}\right) \qquad - 3$$

where Q is the activation energy, T is the absolute temperature, R is the gas constant, and ln k_o is the y intercept of the ln k_p vs. 1/T plot. Activation energies for the oxidation of iron vary from 20 to 47.8 kcal/mole[4,5,6,7]. Using the magnetite rate constant data from Davies, Simnad and Birchenall[7] to plot ln k_p vs. 1/T gives Q = 24.2 kcal/mole and k_o = 4.02 $g/cm^3 min^{-1/2}$, from linear regression. Using these values in Eq 2, with R = 1.987 cal/mole°K, the previously calculated rate constant of $7.932 \times 10^{-7} g/cm^3 min^{-1/2}$ requires a temperature of 516°C.

The above calculations can only be considered approximate. Activation energy for magnetite growth at room temperature has not been accurately determined, and may be considerably higher than the value used, since the diffusion of iron ions becomes much more difficult at

very low temperatures. It has also been suggested[5] that below 200°C the oxidation of iron follows logarithmic kinetics, which give slower oxidation rates than parabolic rate laws. The previous calculations assumed oxidation of iron, and not steel, which typically oxidizes more slowly than pure iron[8,9] (see Appendix). Also assumed was sufficient oxygen for a diffusion limited reaction, while the oxygen concentration in propane is almost negligible, which would greatly reduce the oxidation rate.

While the previously calculated temperature of 516°C is only approximate, it shows that even under ideal oxidation conditions, the growth of a 10 μm thick magnetite layer in the tank service interval requires a temperature considerably higher than the highest temperature the tank would experience in service, unless there is some mechanism present which can either significantly increase the diffusion rate of iron ions in magnetite, or significantly decrease the activation energy required for oxidation at low temperatures.

It has been well established that the presence of sulfur (H_2S, SO_2 or free S) in the oxidation atmosphere can significantly increase the oxidation rate of iron[10,11,12,13,14], while the sulfur content in the steel

itself has been found to have little effect[15]. Atmospheric sulfur increases oxidation by either dissolving in the oxide lattice, or by forming iron sulfides, iron sulfates, or sulfuric acid. Dissolved sulfur in the oxide lattice can increase the defect concentration, which increases ion transport. Iron sulfide stringers in a scale layer act as high diffusion paths for iron ions, with diffusion many orders of magnitude greater than in the pure oxide. If sulfuric acid forms, it can partially dissolve the magnetite, creating acid filled pores which act as high diffusion paths. Typically, sulfuric acid causes the appearance of iron sulfate in aqueous form. Diffusion then changes from slow solid state diffusion, to much quicker aqueous diffusion in the oxide pores.

For the decommissioned tank studied, sulfur assisted oxidation can be ruled out. XRD analysis of the interior oxide layer showed no iron sulfide, EDS analysis showed only traces of sulfur dissolved in the magnetite, and SEM observation of the oxide layer showed a non-porous uniform layer. Also, the propane itself contains sulfur compounds in amounts on the order of only 50 ppm wt.[12], with a maximum of 120 ppm allowed, and only negligible amounts of oxygen and water, which are necessary for the formation of sulfuric acid.

Cracks formed through the oxide layer by oxide stresses can also increase the oxidation rate many orders of magnitude by allowing oxygen direct access to the iron surface. Although many oxide traversing cracks were found in the interior magnetite layer of the studied tank, there was no evidence of fresh oxide formation at the base of the cracks, indicating this mode of oxidation enhancement was not a contributory factor in the oxide layer formation.

The greatest evidence against formation of the oxide layer during tank service is the lack of any oxide layer on either the liquid withdrawal tube, or the 80% outage gage dip tube. Since both of these tubes were constructed from low carbon mild steel, they should have oxidized more rapidly than the low alloy steel tank shell, if oxidation occurred during tank service.

4.3.2 Oxide Formation During Manufacture

Significant evidence exists that leads to the conclusion that the oxide layer was formed during the steel plate manufacturing process itself.

It is very unlikely that the oxide layer was formed in

the manufacture of the tank. At no time during the formation of the tank shell and end caps, were material temperatures sufficiently high to form a 10 μm thick oxide layer in a reasonable time (<6 hours). Since the oxide layer was very uniform across all parts of the tank shell and end caps, it is highly improbable that the oxide was formed during any tank manufacturing welding processes. Also, the completed propane tank was not heat treated as a whole, which discounts the possibility of oxide growth during heat treatment.

The presence of an oxide layer on the outside surface of the tank underneath the factory applied paint, as shown in Figures 14 and 15, which is identical in thickness and composition as the interior oxide layer, shown in Figure 13, immediately suggests the interior oxide layer was also present at the time of manufacture of the tank. The presence of a uniform thickness oxide layer under the steel grade specification paint marking on the inside of the tank shell, as shown in Figures 16, 17, 19, 20 and 21, provides conclusive evidence that the oxide layer was present at the point of steel making, before the tank manufacturing process.

This conclusion is supported by oxidation kinetics. From Eqs 1, 2, and 3, using the previously determined

activation energy, Q and k_o, calculations show that under ideal conditions, a 10 μm thick magnetite layer can be grown in less than 15 minutes, at 1000°C, which are conditions typical of steel rolling.

Typical iron oxidation forms wüstite, magnetite and hematite. The lack of wüstite found in the tank oxide can be easily justified by the high carbon content and alloy additions of the tank steel (see Appendix). The lack of hematite can be explained as follows: At the steel mill, during steel rolling, some abrasive descaling of the steel plate will take place. It has been found that the lack of wüstite, and high content of the more adherent magnetite in a higher carbon steel scale, causes the descaling to be effective in only removing the superficial thin hematite layer, while leaving the bulk of the more adherent magnetite layer intact[16,17].

4.4 OXIDE LAYER SPALLATION

Compressive stresses are generated in oxide layers due to a variety of mechanisms (see Appendix). Typically, the greatest stress is generated during cooling from the different thermal expansion coefficients between oxide

and steel. Excessive compressive stresses in the scale can lead not only to crack formation, but also to oxide spallation.

For a particle of spalled oxide to be released from the oxide/metal interface, through-thickness cracks must form, and adhesion must be lost at the oxide metal interface. Either step can precede the other. Route I spallation occurs if cracks form before adhesion is lost. This is characteristic of oxide systems where the oxide/metal interface is more resistant to fracture than the oxide layer itself. Route II spallation occurs when the interface has lower strength than the oxide, and is characterized by buckling of the oxide before spallation. Figure 25[18] summarizes the different spallation routes.

Spallation of iron oxides can be by both routes. During the oxidation of steel, gaps typically form at points along the metal/oxide interface (see Appendix). Interface strength at the gaps will be non-existent, leading to Route II spallation. At the metal/oxide interface where gaps have not formed, either Route I or Route II spallation can occur depending on how well the oxide is pinned at that location.

Oxide spallation in the decommissioned propane tank

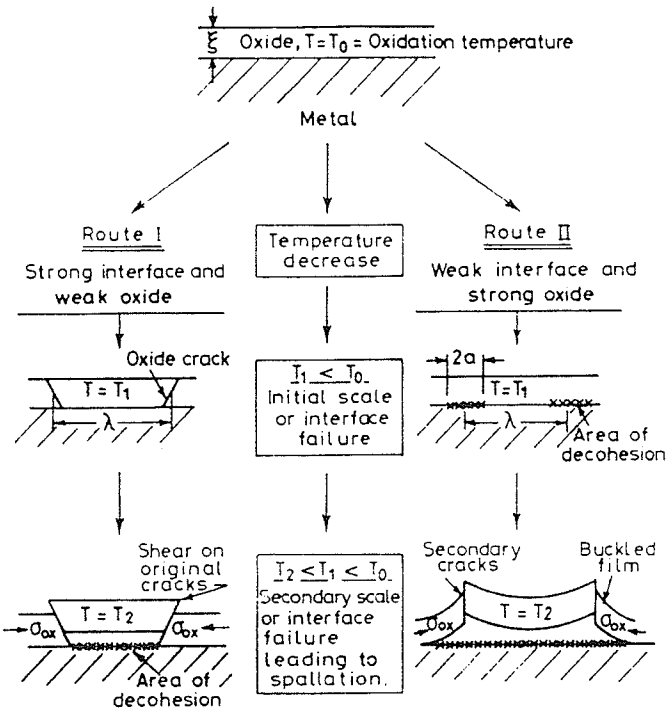

FIGURE 25 Oxide Spallation Routes[18]

appears to be by both routes. Figure 22 shows spallation from the interior tank shell oxide. Oxide buckling, characteristic of Route II spallation, is very evident. Figure 18 shows oxide through-thickness cracking which is characteristic of Route I spallation, before release of the oxide particle.

Spallation of the tank oxide most likely occurs due to strains from weather temperature changes, which add to the already high residual compressive stresses and strains present in the oxide layer from cooling the steel

plate to room temperature after rolling, and from manufacture of the tank.

Rough estimates of these strains, and associated temperature changes, can be made. Reported thermal expansion coefficients for steel[3,18,19,20,21,22,23] vary from 11.7×10^{-6} $^{\circ}C^{-1}$ to 18.1×10^{-6} $^{\circ}C^{-1}$, while the reported coefficients for magnetite[3,23] vary from 5×10^{-6} $^{\circ}C^{-1}$ to 9.3×10^{-6} $^{\circ}C^{-1}$. Choosing an average value of 15×10^{-6} $^{\circ}C^{-1}$ for steel, and 7.2×10^{-6} $^{\circ}C^{-1}$ for magnetite, gives the difference in thermal expansion coefficients, $\Delta\alpha$, as 7.8×10^{-6} $^{\circ}C^{-1}$. Oxide strain due to temperature changes is given by:

$$\varepsilon_t = \Delta\alpha\Delta T \quad - 4$$

Compressive fracture strains for an iron oxide scale are taken from thermal shock tests done by Bruce and Hancock[22], and shown in Figure 25. Extrapolating to room temperature gives a fracture strain of about 1.9×10^{-4}. From Eq

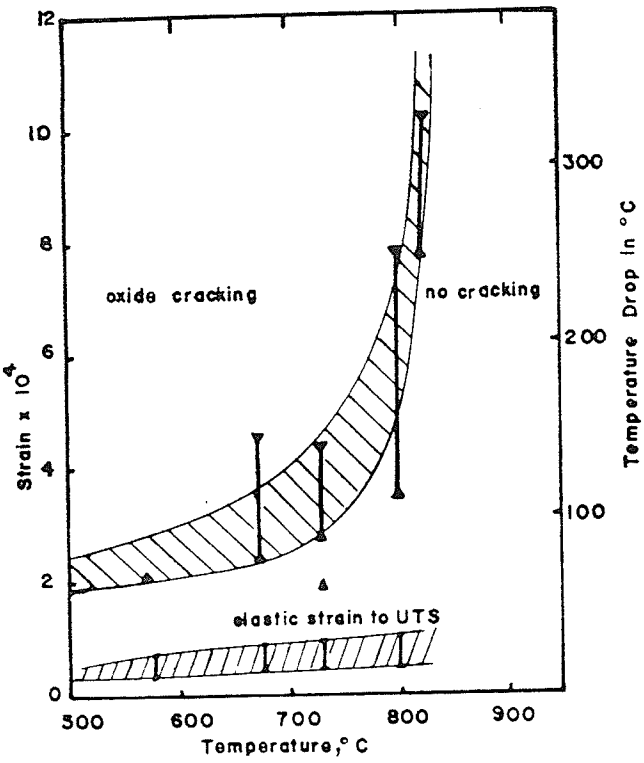

FIGURE 26 Oxide Fracture Strains[22]

4, the required temperature change for oxide fracture at low temperatures is then only 24°C.

While the above calculation can only be considered approximate, even using the extreme values of α = 11.7×10^{-6} $^{\circ}C^{-1}$ for steel, α = 9.3×10^{-6} $^{\circ}C^{-1}$ for magnetite, and a fracture strain of 4×10^{-4} for higher temperatures, requires a temperature change of only 167°C for oxide fracture. This temperature change will be easily exceeded when the steel plate is cooled from rolling temperatures, which accounts for the observation of numerous stress cracks in both interior and exterior oxide layers of the tank.

It is evident from these calculations, that extreme compressive stresses and strains are generated in the oxide layer from cooling the steel plate to room temperature. Additional compressive strains are generated in the interior tank oxide layer from the forming of the tank shell itself. Assuming a nominal tank diameter of 36 cm, and a plate thickness of .277 cm (excluding oxide thickness), rolling the flat steel plate into a cylinder will increase the average compressive strain in the 10 μm thick interior oxide layer by 3.86×10^{-3}, while decreasing that of the exterior tank oxide layer by 3.17×10^{-3}.

The additional compressive strain, and hence temperature decrease, required to spall the oxide after oxide fracture, can not be easily calculated, since the strength of the oxide/metal interface is not known. However, the previous calculations show the extreme compressive strains that may be present in the tank shell interior oxide layer. Any shock or vibration the tank experiences in service, as well as the additional compressive strains which occur between summer and winter temperatures, are likely sufficient to cause spallation.

In fact, increased residue generation, and hence increased oxide spallation, was observed in the DND vehicles which were stored in a heated garage overnight during the winter. The additional spallation was likely caused by the thermal shock experienced by the tank oxide layer on going from 22°C inside the garage, to -25°C outside on a typical Winnipeg winter day.

4.5 RESIDUE GENERATION VS. VEHICLE MILEAGE

Since the magnetic particulate residues are caused by spalling of the propane tank interior oxide layer, and no regrowth of the oxide occurs during tank service, residue generation should decrease with time, and therefore,

mileage of the vehicle. Unfortunately, the DND test failed to provide a great deal of evidence for this conclusion. Most test vehicle filters contained very small amounts of residue, and for many test vehicles, selected filters were lost, mileage documentation on filters was lacking, and the most important early service filters (just after propane conversion) were not available.

Some evidence to support this conclusion does exist, however. Referring to Tables 2 thru 13, residue deposits in the main filters consistently decrease with increasing mileage. Filters 8A and 10A, which were both initial filters, showed the heaviest residue accumulations in the controlled group filters. Other vehicle filters, not in the controlled group, also showed the heaviest deposits in the initial filters.

4.6 SUMMARY

The evidence presented clearly indicates that the black magnetic particulate residues in motor vehicle propane tanks is a result of spallation of an oxide layer on the interior surface of the propane tanks. Furthermore, the oxide layer is formed during the manufacture of the steel

plate from which the tanks are fabricated, and is never completely removed. Indeed, the ASTM specification 7.1.1 for A414 steel[27] states explicitly: "Unless otherwise specified, the material shall be furnished without removing the hot-rolled oxide or scale."

The evidence supporting these conclusions are:

1. Any residue particles larger than 10 μm had to originate within the steel vehicle propane tanks. In the test fleet, all fuel was carefully filtered prior to fueling the vehicles, yet all vehicles generated particulate residues during service, except for the vehicle with an aluminum tank.

2. For the test vehicles, the particulate residue from all the steel tanks was largely oxides of iron (Table 17). Occasionally, traces of weld slag and rust (FeOOH) were detected, which might be expected considering the methods of manufacture of the tank, and the operating conditions.

3. The tank oxide layer was present on the steel from which the tanks were manufactured, and was not formed while the tanks were in service in the motor vehicles.

   a) Calculations show that the oxide thickness of 10 μm observed on the interior tank surface would require an

average operating temperature of about 500°C, clearly not possible.

b) A steel propane tank sectioned and examined after being in service, exhibited an oxide layer on the tank material (Figure 13), but no oxide layer on either the steel liquid withdrawal tube (Figure 11), or the 80% outage gage dip tube (Figure 12). If oxides formed during tank service, all interior steel surfaces would display oxides.

c) The steel grade specification marking found on the inner surface of the tank steel was painted on top of the oxide layer (Figure 19). Therefore, the oxide layer exists on the steel from which the tanks are manufactured.

4. The oxide layer spalls off during service (Figure 22), forming the black magnetic particulate residues which accumulate in the motor vehicle filters.

Conclusions and Recommendations

The magnetic particulate residues found in vehicle propane storage tanks are predominantly flakes of magnetite (iron oxide), which originated in the tank, from spallation of the oxide layer on the interior surface of the tank itself. The oxide layer spallation is likely caused by decreases in temperature (thermal shock) from weather changes, as well as shocks or vibration of the tank during service, which may increase the already extreme residual compressive stresses and strains present in the oxide layer from the manufacturing processes.

The tank oxide layer was found to originate at the point of manufacture of the steel. No regrowth of the tank oxide layer occurs during tank service, and therefore, residue generation in the tank will decrease with increasing mileage of the vehicle.

Elimination of the tank oxide layers would eliminate the generation of magnetic particulate residues within the tanks. Specification ASTM A414[27] allows that the material be furnished with the oxide layer removed. It is therefore recommended that all vehicle propane tanks be manufactured from the descaled steel.

APPENDIX

SUMMARY OF IRON OXIDATION THEORY

The classical oxidation behavior of pure iron will first be discussed, then the effect of the variables of commercial steels will be described.

A.1 Classic Oxidation of Pure Iron in Air or Oxygen[6,7,8,19]

At high temperatures iron will react with oxygen to form a scale of 3 stable parallel layers of iron oxide, arranged in order of oxygen content. The outermost layer having the highest oxygen content is hematite, αFe_2O_3, with a rhombohedral crystal structure; the middle layer magnetite, Fe_3O_4, with a spinel structure; and the innermost layer with the lowest oxygen content is wüstite, FeO, having a simple cubic crystal structure.

Wüstite is only a stable phase above 570°C. Oxidation below 570°C produces only αFe_2O_3 and Fe_3O_4. Oxidation above 570°C with subsequent cooling below the stability temperature for wüstite, causes the FeO to further

oxidize into Fe_3O_4, however the transformation kinetics are diffusion controlled, and with sufficiently quick cooling rates, retained FeO can exist at room temperatures.

Oxide phase stability also depends on oxygen concentration. Figure A.1[7] shows the equilibrium iron-oxygen phase diagram.

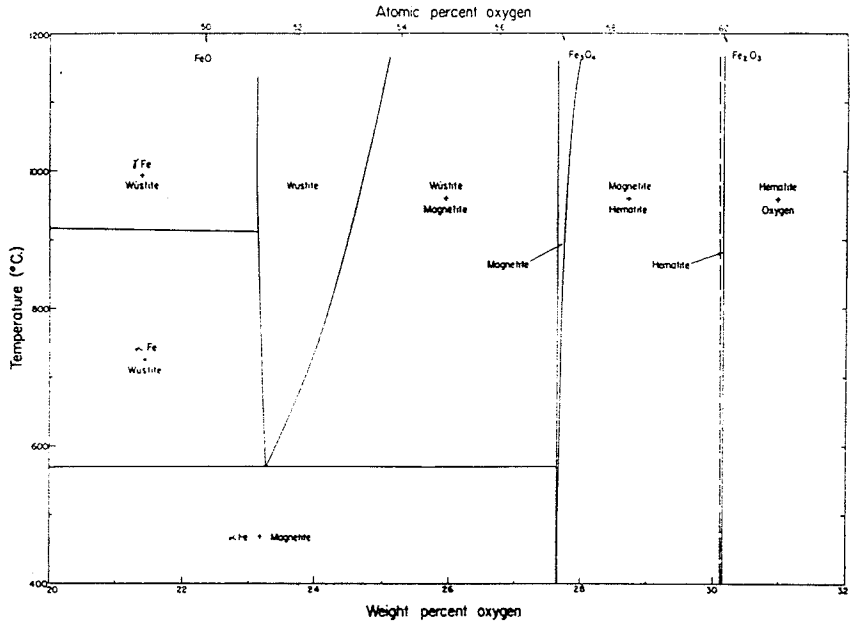

FIGURE A.1 Fe-O Phase Diagram[7]

Both magnetite and wüstite are p-type metal deficit semiconductors with cation vacancies present. Hematite is a metal excess n-type with anion vacancies.

The entire scale grows by diffusion of iron and oxygen.

At the scale/metal interface iron enters the wüstite when cation vacancies become available. Diffusion in magnetite is also by iron ions. In hematite, oxygen is adsorbed at the outer surface of the hematite and is dissolved as soon as an anion vacancy is available. Iron ion diffusion also appears to be significant along hematite grain boundaries.[6,7]

If there is sufficient oxygen available at the outer oxide surface for adsorption, the diffusion of iron ions becomes the rate controlling process. Therefore, at constant temperature, the oxidation rate will decrease with increasing oxide thickness, and oxide thickness can be described by:

$$\frac{dx}{dt} = k_p \frac{1}{x} \qquad \text{- A1}$$

where x is the oxide thickness, k_p is the parabolic rate constant, and t is time.

Integrating gives: $x^2 = \frac{1}{2} k_p t$ - A2

At constant temperature, oxidation then proceeds parabolically with time.

The parabolic rate constant depends on the diffusivity of the diffusing ions in the oxide, and is given by[19]:

$$k_p = \frac{-1}{RT} \int_{\mu'_M}^{\mu^o_M} D_c \, d\mu_M \qquad \text{- A3}$$

where R is the gas constant, T is the absolute temperature, D is the diffusivity of the cations in the oxide, and μ^o_M and μ'_M are the metal chemical potentials at the oxide/gas interface and metal/oxide interfaces, respectively.

The diffusivity follows an Arrhenius relation with temperature, and is given by:

$$D = D_o \exp\left(\frac{-Q}{RT}\right) \qquad \text{- A4}$$

where D_o is the frequency factor, and Q is the activation energy. Since the diffusion of cations is the rate controlling process in the oxidation of iron, the activation energy for oxidation according to[19]:

$$k_p = k_o \exp\left(\frac{-Q}{RT}\right) \qquad \text{- A5}$$

is the same as the activation energy for diffusion of cations in Eq A4.

The oxidation rate of pure iron is not affected by ambient oxygen pressure, provided the oxygen pressure is greater than the dissociation pressure of magnetite. Since the diffusion of cations is the rate controlling process, and the concentration limits of iron ions are

fixed at the metal/wüstite and wüstite/magnetite interfaces, and thus independent of atmosphere, the oxidation rate is therefore independent of oxygen pressure.

The relative equilibrium thicknesses of the 3 oxide layers is proportional to the diffusion rates in each oxide. Wüstite has the greatest cation diffusion, and is therefore the thickest layer. Anion diffusion in hematite is the slowest; hence hematite is the thinnest layer. Under equilibrium conditions, wüstite occupies about 95% of the growing scale layer, magnetite about 4% and hematite about 1%. These proportions change with decreasing temperature, with magnetite becoming thicker, and wüstite becoming thinner.

The reason for the change in relative layer thicknesses is as follows: Since there is a net flow of iron ions outward from the base metal, the oxide layer must recede towards the metal if contact is to be maintained. The only mechanism by which this is possible is creep of the oxide layer. If creep of the oxide is prevented, which is more likely at lower temperatures, contact is lost and gaps appear between the base metal and oxide. Since the iron ions can not traverse the gap, the absorption of ions and diffusion are disrupted. Iron continues to

diffuse out of the wüstite layer until a uniform iron concentration is attained across the wüstite layer corresponding to the equilibrium magnetite concentration, which, along with the slowing of diffusion, leads to the growth of magnetite into the wüstite layer.

During the growth of the scale stresses are developed from the different molar volumes between base metal and oxide, expitaxial misfits, grain boundary oxidation, compositional variations and additional stresses may be created due to surface geometry. Since iron oxides have a greater molar volume than iron, compressive stresses are created as the oxide forms on a fixed surface area. Expitaxial stresses are generated by the misfit between oxide lattice and base metal lattice, but diminish quickly as the oxide thickens[24]. Since grain boundary diffusion is greater than bulk diffusion, oxidation may proceed more quickly in grain boundaries, which creates compressive stresses in the bulk oxide. The compositional variation across the scale due to stoichiometry, which is greatest in wüstite, also creates stresses within the oxide.

Surface geometry greatly affects the oxide growth stresses. Since iron oxidizes by outward cation diffusion, the scale must recede inward towards the base metal to remain in contact with the receding iron

surface. If the oxide grows on a convex surface, the inward recession of oxide will create additional compressive stresses. Oxide growth on a concave surface will reduce compressive stresses, or create tensile stresses at the metal/oxide interface as the oxide attempts to remain in contact with the receding metal surface.

Thermal compressive stresses are typically the greatest residual stresses in scales. As the metal/oxide system is cooled from the reaction temperature, stresses are generated which are directly proportional to the difference in thermal expansion coefficients between the metal and oxide. Since all the iron oxides have lesser thermal expansion coefficients than iron, the generated stresses are compressive in the oxide, and tensile in the metal.

Cracks which may form to relieve the oxide stresses, can provide rapid inward diffusion paths for oxygen. The formation and healing of cracks can then increase the oxidation rate.

A.2 Deviations From Classic Theory For Oxidation of Steel[8,25,26]

Deviations from the classical oxidation theory of pure iron in air or oxygen, are due to carbon content, alloy additions and the differing oxidation atmospheres of commercial steels. In general, the oxidation rate of steel is much slower than that of pure iron.

Alloy addition and atmospheric oxidation effects are complex, and a full description of all the variables is beyond the scope of this brief summary, so the reader is referred to reference 8 for a comprehensive discussion. Only a brief summary will be given here.

The presence of carbon forms a gaseous reaction product during oxidation, which causes oxidation rates to be more erratic. Gas pressure in discontinuities can cause cracking, leading to increased rates of oxidation. Alternatively, gas products in gaps and fissures can interfere with the healing of these voids, leading to a reduction in oxidation rate.

Alloy additions can have various effects on the oxidation of steels. Phosphorus typically lowers the oxidation resistance in steel slightly, while sulfur, at the levels

normally present in steels, typically has no effect on oxidation. Manganese can substitute for iron in wüstite and magnetite, but oxidation effects directly due to manganese are only slight. Generally, alloy additions reduce the oxidation rate by inhibiting dislocation movements at the metal/oxide interface, which promotes the formation of gaps and pores, which further inhibits iron diffusion.

Silicon, if present in amounts greater than .25%, can form separate phases in the scale, usually pools and extended stringers of iron manganese silicate. In steels with higher silicon content, a thin film of silica may form at the iron/oxide interface which interferes with the diffusion of cations, leading to greatly reduced oxidation rates.

Alloying elements more noble than iron may lead to surface enrichment of alloying additives, which can affect cation diffusion. Enrichment of copper in the surface layer may also lead to the precipitation of molten metallic copper, which can cause intergranular attack, hot-shortness and surface defects.

Although the oxidation rate of pure iron is independent of oxygen pressure, the oxidation rate of steel decreases

with decreased oxygen pressure. The reason is likely due to the carbon additions in steel, which cause scale separation and pore formation more readily.

The presence of steam typically increases the oxidation rate. The scale formed in steam is more plastic, creeps more readily and therefore does not form a gap as readily. Also, gas reactions in the pores permit oxygen transport across the scale, thus counteracting the disruption of the diffusion path. A similar but weaker effect is produced by the presence of CO_2 in the oxidizing gases.

Because of the formation of gaps and pores at the metal/oxide interface in steels oxidized in air or oxygen, wüstite formation is suppressed, and the magnetite layer will predominate.

REFERENCES

1. R. J. Falkiner, PGAC Odourant and Residue Committee Memorandum, 27 May 1987.
2. A. C. Davies, The Science and Practice of Welding, 7th ed., Cambridge University Press, Cambridge, 1977.
3. "The Oxide Handbook", IFI/Plenum, New York, 1973.
4. V. I. Arkharov et al., Dop. Akad. Nauk Ukrain. RSR, Jan. 1975, [A], (1), 73-75.
5. M. J. Graham, S. I. Ali, and M. Cohen, J. Electrochem. Soc., Apr. 1970, **117**, (4), 513-516.
6. D. Caplan, R. J. Hussey, G. I. Sproule, and M. J. Graham, Corr. Sci., **21**, 9, 689-711, 1981.
7. M. H. Davies, M. T. Simnad, and C. E. Birchenall, J. of Metals, **3**, 889, (Oct. 1951).
8. K. Sachs, and C. W. Tuck, Proceedings of the Conference on Reheating for Hot Working, Iron and Steel Inst., 1968, 1-17.
9. J. Manenc, and G. Vagnard, Corr. Sci., Dec. 1969, **9**, (12), 857-868.
10. I. A. Montil'no, et al., Zhur. Priklad. Khim., 1969, **42**, (3), 488-496.
11. V. A. Feoktistov, et al., Chem. Tech. Fuels and Oils, v21, n7-8, Jul-Aug. 1985, 394-397.
12. A. F. Williams, and W. L. Lom, Liquefied Petroleum Gases, New York, John Wiley & Sons Inc., 1974.

13. D. P. Whittle, "Introductory Remarks on Corrosion", Proceedings Corrosion/Erosion of Coal Conversion Systems Materials Conference, Jan. 1979, NACE, Houston, 218-221.

14. H. Kaesche, Metallic Corrosion, NACE, Houston, 1985.

15. B. Hammar, and N. G. Vannerberg, Scand. J. Metallurgy, 1974, 3, (4), 173-176.

16. V. I. Rospasienko, and V. S. Chernitsym, Stal', May 1969, (5), 427-430.

17. A. A. Bagrov et al., Liteinoe Proizvod., June 1976, (6), 31-33.

18. H. E. Evans, and R. C. Lobb, Corr. Sci., 24, 3, 202-222, 1984.

19. S. A. Bradford, "Fundamentals of Corrosion in Gases", ASM Metals Handbook, vol 13, 9th ed. ASM International, USA, 1987.

20. F. P. Beer and E. R. Johnston Jr., Mechanics of Materials, New York, McGraw-Hill Inc., 1981.

21. "Handbook of Chemistry and Physics", 71st ed., 1990-91, CRC Press Inc., USA.

22. D. Bruce, and P. Hancock, J. Inst. of Metals, 1969, 97, 148-155.

23. B. M. Gugelev and A. I. Rytvinsky, Prot. Metals, 1970, 6, 1, 112-113.

24. J. V. Cathcart, and R. E. Pawel, "The Mechanical Behavior of Oxide Scales", Proceedings Corrosion/Erosion of Coal Conversion Systems Materials Conference, Jan. 1979, NACE, Houston, 300-329.

25. Norman L. Peterson Memorial Symposium on "Oxidation of Metals and Associated Mass Transport", Metallurgical Soc., 1987.

26. J. Baud et al., Centre Document Siderurgique Circul. Inform. Techn., 1973, **30**, (1), 49-59.

27. Annual Book of ASTM Standards, 1986, vol. 1.03, ASTM, 1986.